

**Theoretical investigation of contact-induced phenomena in
composite materials containing fullerenes and nanotubes
deposited on ferromagnetic substrates**

Evgenia A. Kovaleva

Siberian Federal University 2016

ABSTRACT

Exploring new spin filtering materials is an important issue of modern spintronics. Conducting spin-polarized current, these materials may be implemented in magnetoresistive memory elements, hard disk scanning heads, and other devices. Previously it was shown that planar hexagonal nanostructures such as graphene and *h*-BN have great potential for being used in spintronic devices due to the spin polarization induced by the contact with ferromagnetic substrate. It is reasonable to suppose that boron nitride and carbon nanotubes (BNNTs and CNTs) can also be used for this purpose. Although the contact interaction of carbon and BN nanotubes with ferromagnetic substrates is supposed to be quite similar to that of the corresponding graphene and *h*-BN hexagonal monolayers, which can be considered as nanotubes of extremely large diameter, finite thickness of the tubes can result in a significant change of interface properties. This effect has not been investigated in detail.

The interaction of zigzag and armchair carbon and boron nitride nanotubes (NT) with ferromagnetic transition metal (TM) surfaces, namely, Ni(111) and Co(0001), was studied within the framework of density functional theory. Different configurations of composite compartments mutual arrangement were considered. All NT(*n*,0)/Co interfaces were found to be more energetically favorable than NT(*n*,0)/Ni, and conductive carbon nanotubes demonstrate slightly stronger bonding than semiconducting ones. Partial densities of states and spin density spatial distribution of optimized structures were investigated. Influence of ferromagnetic substrate on nanotubes' electronic properties was discussed. The presence of contact-induced spin polarization was established for all nanocomposites. The contact-induced polarization of BNNT resulted in the

appearance of local conductivity in the vicinity of the interface while the rest of the nanotube lattice remained to be insulating.

Organic-based spintronics is one of the most fast-developing fields in nanoelectronics. Buckminsterfullerene-based composites are widely investigated due to their unique properties and there are a number of studies on their interaction with various types of substrates. Ferromagnetic surfaces are of a particular interest for potential spintronics applications. Based on the data reported in literature, one can suppose that there is more than one stable structure in $C_{60}/Fe(001)$ composite system. Different possible adsorption sites of C_{60} molecule were investigated revealing the possibility of their coexistence and its influence on the composite properties.

Half-metallic $La_{0.7}Sr_{0.3}MnO_3$ (LSMO) is widely used in spintronic devices due to its high spin polarization. It has a lot of advantages comparing with conventional ferromagnetic materials (e.g. Fe, Co, Ni) which are much less spin polarized and suffering from well-known conductivity mismatch problem. Using half-metallic electrodes (LSMO) allows achieving up to 95% contact spin polarization in MTJ devices without using any additional layers. Moreover, in contrast to the above mentioned transition metals, LSMO is highly resistive against oxidation. These features make LSMO an ideal candidate to be used in spintronics.

Atomic and electronic structures of LSMO-based composites with carbon nanotubes were studied within the framework of density functional theory with respect to the termination of LSMO surface. The deformation of tubes caused by the lattice mismatch with the substrate resulted in a major change in their electronic structure. The surface terminated with Mn-O layer provided much stronger interaction with carbon nanotubes than Sr-O terminated one did. The interaction with transition metal atoms was essential for forming nanocomposites when nanotube structure was visibly distorted.

Spinterface between fullerene C₆₀ and La_{0.7}Sr_{0.3}MnO₃ (LSMO) was studied within the framework of density functional theory. As previously, co-existence of many different configurations was shown, and probabilities of their appearance were estimated. Dependence of composite properties on configuration and temperature was also investigated. Key role of transition metal atoms in both binding between composite compartments and magnetic ordering in C₆₀ molecule was discussed. The latter was suggested to be responsible for spin-polarized charge transport while overall magnetic moment of fullerene molecule was relatively small.

LIST OF THE ARTICLES PUBLISHED

1. Kuzubov, A.A. Contact-induced spin polarization in BNNT(CNT)/TM (TM=Co, Ni) nanocomposites / A.A. Kuzubov, E.A. Kovaleva, P. Avramov, A.V. Kuklin, N.S. Mikhaleva, F.N. Tomilin, S. Sakai, S. Entani, Y. Matsumoto, H. Naramoto // Journal of Applied Physics. - 2014. - Vol. 116. - 084309.
2. Kuzubov, A.A. On the possibility of contact-induced spin polarization in interfaces of armchair nanotubes with transition metal substrates / A.A. Kuzubov, E.A. Kovaleva, F.N. Tomilin, N.S. Mikhaleva, A.V. Kuklin // Journal of Magnetism and Magnetic Materials. - 2015. - Vol. 396. - P. 102–105.
3. Kuzubov, A.A. Buckminsterfullerene's movability on the Fe(001) surface / A.A. Kuzubov, E.A. Kovaleva, P.V. Avramov, A.S. Kholtobina, N.S. Mikhaleva, A.V. Kuklin // Journal of Magnetism and Magnetic Materials. – 2016. – Vol. 410. – P. 41-46.
4. Kovaleva, E.A. Characterization of LSMO/C60 spinterface by first-principle calculations / E.A. Kovaleva, A.A. Kuzubov, P.V. Avramov, A.V. Kuklin, N.S. Mikhaleva, P.O. Krasnov // Organic electronics. - 2016. - Vol. 37. - P. 55-60.

TABLE OF CONTENTS

1. Theoretical background	7
1.1 Density functional theory	7
1.1.1 Local density approximation, generalized gradient approximation	8
1.1.2 DFT-D3 method [8]	10
1.1.3 Hubbard U method for systems with strong electron correlations [18]	11
1.2 Plane wave basis set	12
1.2.1 Pseudopotential approach	13
1.2.2 Projector augmented wave method	15
1.3 Methods for geometry optimization	16
1.3.1 Conjugated gradient method	18
1.4 Methods for transition state evaluation	18
1.4.1 Nudged elastic band method	18
2. Interfaces of nanosized objects with magnetic substrates as promising spin filtering materials	21
3. Computational methods	27
3.1 Study of NT interfaces with transition metal surfaces	27
3.2 Study of C ₆₀ /Fe(001) nanocomposite	29
3.3 Study of LSMO-based nanocomposites	30
4. Results and discussion	33
4.1 Interaction between carbon and boron nitride nanotubes and ferromagnetic Co(0001) and Ni(111) substrates	33
4.2 Buckminsterfullerene C ₆₀ interfaces with Fe(001) surface	42

4.3	Characterization of LSMO/C ₆₀ nanocomposites	52
4.4	The role of surface termination in CNT/LSMO composites	59
4.4.1	Interaction with Sr-O terminated surface	59
4.4.2	Interaction with Mn-O terminated surface	64
	Summary	67
	References	69

1. THEORETICAL BACKGROUND

1.1 Density functional theory

Density functional theory (DFT) method is based on the Hohenberg-Kohn theorem [1] establishing the relation between the electron density of system ρ and its electron energy so the energy of electronic ground state is fully determined by the electron density. The proof of Hohenberg and Kohn theorem was then extended to satisfy arbitrary temperature systems by Mermin [2]. However, these pioneer works didn't propose a particular recipe to construct the functional itself. Introducing the orbital approximation, Kohn and Sham made the explicit usage of density functional theory possible in computational chemistry [3,4].

Total energy functional can be presented as:

$$E[\rho(\vec{r})] = T[\rho(\vec{r})] + U_{ee}[\rho(\vec{r})] + \int \rho(\vec{r}) V_{ee}(\vec{r}) d\vec{r}, \quad (1)$$

where $T[\rho(\vec{r})]$ is the term for electrons' kinetic energy; $U_{ee}[\rho(\vec{r})]$ stands for the energy of electron-electron interaction; and $V_{ee}(\vec{r})$ is the potential describing the interaction between electrons and external field. Minimizing the energy with respect to the one-electron orbitals, one can obtain Kohn-Sham equations similar to the Hartree-Fock equations:

$$h_{ks}\varphi_i = \left(-\frac{1}{2}\nabla^2 + V_{ne}(r) + \int \frac{\rho(r')}{|r-r'|} dr' + v_{xc}(r) \right) \varphi_i = \varepsilon_i \varphi_i, \quad (2)$$

where h_{ks} is one-electron Kohn-Sham operator similar to the Fock operator in Hartree-Fock equations; ε_i is the energy of canonical one-electron Kohn-Sham orbitals; φ_i is one-electron canonical Kohn-Sham orbital; V_{ne} stands for the potential of nuclei-electron interaction; and v_{xc} is exchange-correlation potential.

Density functional approximations differ from each other by the exact form of exchange-correlation functional. It's usually described through the exchange-correlation energy density ε_{xc} :

$$V_{xc}(r) = \frac{\partial E_{xc}[n]}{\partial n(r)} = \varepsilon_{xc}[n(r)] + n(r) \frac{\partial \varepsilon_{xc}(r)}{\partial n}. \quad (3)$$

Exchange-correlation density ε_{xc} can be, in turn, presented as the sum of correlation ε_c and exchange ε_x energy.

1.1.1 Local density approximation, generalized gradient approximation

Local density approximation (LDA) [5] assumes that the electron density can be locally presented as homogeneous electron gas, or, in other words, the electron density is described by the smooth function. In more general approach, local spin density approximation (LSDA) is used for α and β densities being different from each other. Exchange-correlation potential is constructed following the equation:

$$V_{xc}^{LDA} = \int dr E_{xc}(n(r))n(r), \quad (4)$$

where E_{xc} is one-particle exchange-correlation energy of homogeneous electron gas. Exchange part of this energy was originally calculated as:

$$E_x(n) = -\frac{0,458}{r_s(n)}, \quad (5)$$

where $r_s(n) = \left(\frac{3}{4\pi n}\right)^{1/3}$

Correlation energy for homogeneous gas was originally derived as:

$$E_c(n) = -\frac{0,44}{r_s(n) + 7,8}. \quad (6)$$

Interpolation allows one to obtain the equation suitable for any density:

$$E_{xc}(n) = -\frac{1,222}{r_s(n)} - 0,066 \ln \left(1 + \frac{11,4}{r_s(n)} \right). \quad (7)$$

There are lots of extensions and further developments of LDA approach. Still, this approximation is used quite frequently since it is suitable for many systems, including ones with weak van-der-waals interactions.

In order to improve local density approximation, one should consider inhomogeneous electron gas which can be achieved by introducing the gradient of exchange and correlation energies. This approach is known as the generalized gradient approximation (GGA) method. One of the most used functionals for calculations in periodic boundary conditions is Perdew–Burke–Ernzerhof (PBE) functional [6].

Exchange energy is generally described in GGA as

$$E_{XC}^{GGA}[n_{\uparrow}, n_{\downarrow}] = \int d^3r n [\varepsilon_c^{unif}(r_s, \xi) + H(t, r_s, \xi)], \quad (8)$$

where ε_c^{unif} is one-particle correlation energy of homogeneous electron gas; r_s is the local Seitz radius $\left(n = \frac{3}{4\pi r_s^3} = \frac{k_f^3}{3\pi^2}\right)$; $\xi = (n_{\uparrow} - n_{\downarrow})/n$ is spin polarization; and $t = |\nabla n|/2\phi k_s n$ is the density gradient. Here $\phi(\xi) = \frac{((1+\xi)^{2/3} + (1-\xi)^{2/3})}{2}$ is the spin scaling [7]; $k_s = \sqrt{4k_f/\pi a_0}$ is the Thomas-Fermi screening; $k_f = (3\pi^2 n)^{1/3}$, $a_0 = \hbar^2/me^2$ is the first Bohr radius.

The gradient supply H is described within the framework of PBE as:

$$H = (e^2/a_0)\gamma\phi^3 \ln \left\{ 1 + \frac{\beta}{\gamma} t^2 \left[\frac{1+At^2}{1+At^2+A^2t^4} \right] \right\}, \quad (9)$$

where

$$A = \frac{\beta}{\gamma} \left\{ \exp \left[\frac{-\varepsilon_c^{unif}}{(e^2/a_0)\gamma\phi^3} - 1 \right] \right\}^{-1}. \quad (10)$$

Thus, PBE exchange term is determined by the following restrictions:

1) when $\xi = 0$

$$E_X^{GGA} = \int d^3r n \varepsilon_x^{unif}(n) F_X(s), \quad (11)$$

where $\varepsilon_x^{unif} = -\frac{3e^2 k_f}{4\pi}$;

2) exact exchange energy is equal to:

$$E[n_\uparrow, n_\downarrow] = (E_X[2n_\uparrow] + E_X[2n_\downarrow])/2; \quad (12)$$

3) linear response function $F_X(s)$ is:

$$F_X(s) \rightarrow 1 + \mu s^2, \quad (13)$$

when $s \rightarrow 0$, $\mu = 0.21951$ (this term accounts for the exchange without correlation); $s = |\nabla n|/2k_f n$ is the density gradient;

4) the condition

$$E_X[n_\uparrow, n_\downarrow] \geq E_{XC}[n_\uparrow, n_\downarrow] \geq -1,679e^2 \int d^3r n^{4/3} \quad (14)$$

is satisfied when spin-polarized $F_X(\xi = 1, s) = 2^{1/3} F_X(s/2^{1/3})$ smoothly increases from s up to the maximum being equal or less than 2.273, which means that $F_X(s) \leq 1.804$.

So the simplest form of $F_X(s)$ satisfying 4 and 3 is[6]:

$$F_X(s) = 1 + k - k/(1 + \mu s^2/k), \quad (15)$$

where $k = 0,804$.

1.1.2 DFT-D3 method [8]

One of the acute issues in modern DFT is the way to describe weak van-der-waals interactions. A large number of works is devoted to this problem [8–17]. Considering this issue in terms of the accuracy and computational efficiency, long-

range empirical corrections to the standard functionals are supposed to be more convenient for practical use. DFT-D3 is one of the most widely used and well-tested approaches.

Total energy in DFT-D3 method is determined as:

$$E_{DFT-D3} = E_{KS-DFT} - E_{disp}, \quad (16)$$

where E_{KS-DFT} is conventional DFT total energy, and E_{disp} is dispersion correction:

$$E_{disp} = -1/2 \sum_{i=1}^{N_{at}} \sum_{j=1}^{N_{at}} \sum_L \left(f_{d,6}(r_{ij,L}) \frac{C_6^{ij}}{r_{ij,L}^6} + f_{d,8}(r_{ij,L}) \frac{C_8^{ij}}{r_{ij,L}^8} \right). \quad (17)$$

Here N_{at} stands for the number of atoms, C_n^{ij} is n order dispersion constant for ij atomic pair, r_{ij} is interatomic distance. Damping function $f_{d,n}$ is necessary for avoiding inaccurate description of small r region:

$$f_{d,n}(r_{ij}) = \frac{s_{r,n}}{1 + 6(r_{ij}/(s_{r,n}R_{0ij}))^{-\alpha_n}}, \quad (18)$$

where $s_{r,n}$ is order-dependent scaling, R_{0ij} stands for cutoff radius, and α_n is steepness.

1.1.3 Hubbard U method for systems with strong electron correlations [18]

Most of conventional DFT functionals suffers from the strong electron density delocalization which is suitable for many systems but fails to describe Mott insulators and other compounds with localized electrons.

Hubbard approach (DFT+U) is one of the simplest way to account for strong electron correlations. The main idea behind this method is to describe strongly localized d and f -electrons using Hubbard model which is the extension of tight-binding approach, while valence electrons are described by conventional DFT:

$$E_{LDA+U}[\rho(r)] = E_{LDA}[\rho(r)] + E_{Hub}[\{n_{mm'}^{lq}\}] - E_{dc}[\{n^{lq}\}], \quad (19)$$

where E_{LDA} is the energy obtained using local density approximation; E_{Hub} is correlated states energy; E_{dc} is the double-counting term since they are accounted both by the Hubbard correction and conventional calculation:

$$E_{dc}[\{n_{mm'}^l\}] = \sum_I \left\{ \frac{U^I}{2} n^I (n^I - 1) - \frac{J^I}{2} [n^{I\uparrow} (n^{I\uparrow} - 1) + n^{I\downarrow} (n^{I\downarrow} - 1)] \right\}. \quad (20)$$

Here U and J are constants for Coulomb and exchange interaction manually chosen in order to better represent experimental data; n stands for localized orbitals occupation. Dudarev et al. [19] proposed to use effective U parameter ($U_{eff} = U - J$) instead.

1.2 Plane wave basis set

According to the Bloch's theorem, eigenvalues of one-electron Hamiltonian with periodic potential with the period of lattice can be chosen to be the product of the plane wave and the periodic function of the same period:

$$\psi_i = \exp[ik \cdot r] f_i(r), \quad (21)$$

where k is the wave vector, $f_i(r)$ is the periodic function:

$$f_i(r) = f_i(r + l). \quad (22)$$

Local part of the wave function can be expanded using plane waves basis set with wave vectors equal to the vectors of reciprocal crystal cell:

$$f_i(r) = \sum_G c_{i,G} \exp[iG \cdot r], \quad (23)$$

where reciprocal cell vectors G are derived from $G \cdot l = 2\pi m$ for each l (unit cell vector), m is the integer. Thus, each wave function can be presented as the sum of plane waves:

$$\psi_i(r) = \sum_G c_{i,k+G} \exp[i(k + G) \cdot r]. \quad (24)$$

It's worth noting that $c_{i,k+G}$ are more important for smaller kinetic energies $(\hbar^2/2m)|k + G|^2$ than for ones with higher energy. Thus, one can choose the cutoff energy in order to include only plane waves with kinetic energy lower than cutoff. This approximation lead to inaccuracy of the total energy which can be reduced by the cutoff energy increasing.

Combining (24) with the Kohn-Sham equation (2) and integrating lead to:

$$\sum_{G'} \left[\frac{\hbar^2}{2m} |k + G|^2 \delta_{GG'} + V_{ion}(G - G') + V_H(G - G') + V_{XC}(G - G') \right] \cdot c_{i,k+G} = \varepsilon_i c_{i,k+G}. \quad (25)$$

Here the first term accounts for the kinetic energy of electrons, V_{ion} is ion-electron static potential, V_H is Hartree electron potential, and V_{XC} is exchange-correlation potential. The size of matrix is determined by the plane waves cutoff energy $(\hbar^2/2m)|k + G_c|^2$. It's going to be larger for systems with valence and core electrons. Using pseudopotential approach [20,21], one can expand wave functions to the smaller set of plane waves.

1.2.1 Pseudopotential approach

The main idea behind the pseudopotential approach is to calculate explicitly only valence electrons while keeping the core electrons the same as for individual atoms [22]. These core electrons affect only the effective ion charge.

Practically, this means that strong ion-electron potential is substituted by a weaker pseudopotential describing all valence electrons properties. The real system is thus substituted by the pseudoions and pseudovalence electrons. The pseudoion potential matches the real ion potential outside the cutoff radius r_c but it's much weaker within this radius. The Schrodinger equation is solved easier within the sphere of r_c radius since the wavefunction is expanded to a smaller set of basis functions.

There are four general criteria for pseudopotential construction [23]:

- 1) pseudowavefunction should be nodeless in order to obtain smooth wavefunction;
- 2) charge within the sphere of r_C radius should be the same for both wave functions;
- 3) pseudowavefunction should be continuous and twice differentiable;
- 4) eigenvalues of wave functions should be equal.

Generally, pseudopotentials are determined as:

$$V_{NL} = \sum_{lm} |lm\rangle V_l \langle lm|, \quad (26)$$

where $|lm\rangle$ are spherical harmonics, V_l is pseudopotential acting on the wave function with angular moment l .

DFT method with plane wave basis set and pseudopotentials is the most efficient tool for computational chemistry and material science [22,24].

One of the first derived pseudopotential methods was norm-conserving pseudopotential [25,26]. All-electron (AE) wave function is substituted by the smooth nodeless pseudowave function (PS) within the core radius. The only restriction for the choice of PS is the norm-conserving condition: PS wave function has to have the same norm within the chosen radius as the AE one. Outside the core radius, PS and AE wave functions are identical. For accurate description of charge distribution the cutoff radius should be close to the maximum of AE wave function [27]. Hence, large plane wave basis set is demanded for elements with localized orbitals. Increasing of the cutoff radius is usually not an appropriate solution since it leads to the worse matching between AE and PS.

One of the most successful approaches is the ultrasof pseudopotential method (US-PP) proposed by Vanderbilt [28]. The norm-conserving condition can be relaxed when solving generalized eigenvalue problem so the only condition is

the match between AE and PS wave functions at the cutoff radius. This allows choosing it to be far from the AE maximum.

In order to compensate the charge deficit, valence electron charge density is determined as:

$$n_v(r) = \sum_{n,k} \phi_{nk}^*(r) \phi_{nk}(r) + \sum_{i,j} \rho_{ij} Q_{ji}(r), \quad (27)$$

where

$$\rho_{ij} = \sum_{n,k} \langle \beta_i | \phi_{nk} \rangle \langle \phi_{nk} | \beta_j \rangle, \quad (28)$$

$$Q_{ij}(r) = \psi_i^*(r) \psi_j(r) - \phi_i^*(r) \phi_j(r), \quad (29)$$

ψ_j and $\phi_j(r)$ correspond to all-electron and pseudowave functions, β_i are local wave functions.

1.2.2 Projector augmented wave method

Projector augmented wave method (PAW) is the natural extension of both ultrasoft pseudopotential approach (US-PP) and linearized augmented-plane-wave method (LAPW) [29]. On the one hand, it's more generalized form of LAPW since all-electron wave functions are considered like in other augmented wave methods. On the other hand, many operations being performed are very similar to the ones used within the pseudopotential framework. The only difference between US-PP and PAW is the presence of one-center terms in latter case [30]. Along with that, PAW is still all-electron method. All-electron (AE) wave function is described following the methodology of augmented wave methods being linearly connected to the pseudowave function (PS):

$$|\psi_n\rangle = |\tilde{\psi}_n\rangle + \sum_i (|\phi_n\rangle - |\tilde{\phi}_n\rangle) \langle \tilde{p}_i | \tilde{\psi}_n \rangle, \quad (30)$$

where $|\psi_n\rangle$ and $|\tilde{\psi}_n\rangle$ correspond to AE and PS wave functions, partial AE wave functions $|\phi_n\rangle$ are constructed by the radial integration of Schrodinger equation and further orthogonalization with respect to the core states, partial PS wave functions $|\tilde{\phi}_n\rangle$ coincide the corresponding $|\phi_n\rangle$ outside the augmentation region and construct the full set within this region, $\langle\tilde{p}_i|$ is the projector function localized in augmentation region and satisfying the equation:

$$\langle\tilde{p}_i|\tilde{\phi}_j\rangle = \delta_{ij}. \quad (31)$$

Partial wave functions are the product of spherical harmonics and radial meshed functions. Projectors are constructed in the same way and presented as the plane waves set, similarly to PS functions.

Core levels are described as:

$$|\psi^c\rangle = |\tilde{\psi}^c\rangle + |\phi^c\rangle - |\tilde{\phi}^c\rangle, \quad (32)$$

with no projector functions used.

1.3 Methods for geometry optimization

The problem of finding the minimum of the function f is equivalent to the problem of finding its gradient g node. Most of geometry optimization methods are based on well-known Newton method proposing the recipe for numerical solvation of the $f(x)=0$ as:

$$x_{i+1} = x_i - \frac{f(x_i)}{f'(x_i)}, \quad (33)$$

For the optimization problem the equation (33) turns into:

$$(x_{i+1} - x_i) = -\frac{g_i}{H_i} = -H_i^{-1}g_i, \quad (34)$$

where g stands for gradient vector, and H is the hessian.

Newton-Raphson method is the improvement of original Newton method by choosing the optimal step after several iterations. Using (34) can lead to

situation when Taylor's expansion is not correct. Introducing the bias-correction allows controlling the direction and step in the right part of the eq. (34):

$$(x_{i+1} - x_i) = -\lambda_i H_i^{-1} g_i, \quad (35)$$

where $\lambda_i = \arg \min_{\lambda} f(x_i - \lambda_i H_i^{-1} g_i)$.

Analytical calculation of first energy derivatives is necessary for Newton-Raphson optimization. Hessian can be estimated either analytically or numerically. The family of quasi-Newton methods uses iteration procedure of hessian updating. One of the most frequently used schemes for such updating is the one proposed by Broyden, Fletcher, Goldfarb and Shanno (BFGS) [31–34]:

$$\begin{aligned} & (H^{(n)})^{-1} \\ &= (H^{(n-1)})^{-1} + \frac{\langle \Delta x^{(n)} | \Delta g^{(n)} \rangle + \langle \Delta g^{(n)} | (H^{(n-1)})^{-1} | \Delta g^{(n)} \rangle}{(\langle \Delta x^{(n)} | \Delta g^{(n)} \rangle)^2} \cdot |\Delta x^{(n)} \rangle \langle \Delta x^{(n)}| \\ & \quad - \frac{(H^{(n-1)})^{-1} | \Delta g^{(n)} \rangle \langle \Delta x^{(n)}| + |\Delta x^{(n)} \rangle \langle \Delta g^{(n)} | (H^{(n-1)})^{-1}}{\langle \Delta x^{(n)} | \Delta g^{(n)} \rangle}, \end{aligned} \quad (36)$$

where $\Delta g^{(n)} = g^{(n)} - g^{(n-1)}$, $\Delta x^{(n)} = x^{(n)} - x^{(n-1)}$, $(H^{(0)})^{-1} = E$.

The BFGS scheme implementation may lead to the negative Hess matrix eigenvalues which means the optimization of saddle point rather than energy minimum. Rational function (RF) approach allows avoiding this situation. Hessian is now calculated as:

$$H^{(n)} = H^{(n-1)} + \frac{|\Delta g^{(n)} \rangle \langle \Delta g^{(n)}|}{\langle \Delta x^{(n)} | \Delta g^{(n)} \rangle} - \frac{H^{(n-1)} |\Delta x^{(n)} \rangle \langle \Delta x^{(n)} | H^{(n-1)}}{\langle \Delta x^{(n)} | H^{(n-1)} | \Delta x^{(n)} \rangle}, \quad (37)$$

where $H^{(0)} = E$.

1.3.1 Conjugated gradient method

Conjugated gradient method belongs to the family of local optimization methods. It's widely used for geometry optimization because of its fast convergence and high reliability. The main idea behind the method is the construction of conjugated directions on the base of gradient values.

The bias direction at the iteration i is determined with respect to the previous one using the equation:

$$\vec{S}_i = -g_i + w_i \cdot \vec{S}_{i-1}, w_i = \frac{\|g_i\|^2}{\|g_{i-1}\|^2}. \quad (38)$$

1.4 Methods for transition state evaluation

When searching for the saddle point, one has to use methods allowing simultaneous maximization of one degree of freedom and minimization of the others. One way to do this is to use quasi-Newton algorithms for searching the energy maximum along the lowest vibrational mode of system. Still, this method demands the initial structure of transition state to be close enough to the real one. This, in turn, leads to additional calculations for scanning the potential energy surface in order to find the geometry close to the transition state.

1.4.1 Nudged elastic band method

The most reliable method for finding minimum energy path (MEP) of reaction is the nudged elastic band method (NEB). Each image along the path corresponds to the energy minimum in any direction perpendicular to the path.

NEB is a chain method [35,36] which uses a number of geometry images to describe the reaction path. MEP calculation starts from the construction of images corresponding to the intermediate states of the system (4-20 images). Using

internal coordinates interpolation is reasonable in many cases, for example, if the rotational motion is involved [37]. Images are bound to each other by elastic band ensuring the continuity of path during the calculation and equal spacing between them. The optimization of constructed structures results into MEP.

The main feature of NEB distinguishing it from other elastic band methods is a special way to project forces in order to divide supplies from elastic forces and potential forces acting on atoms. Calculation of tangent for each image at each iteration allows obtaining parallel and perpendicular components of forces. Only the component of elastic force parallel to the path and only the component of potential force perpendicular to the path lead to that elastic band affects only the image spacing and not the MEP convergence. Otherwise, the interaction between forces lead to the shift of images and prevents MEP from following the curve shape [38,39]. NEB allows altering elastic forces without shifting of images. Tangent to the reaction path \hat{t} is the normalized vector to the higher energy configuration or the weighted average of two neighboring configurations in the vicinity of maximum. So, the force acting on configuration i consists of two independent components:

$$F_i^{NEB} = F_i^\perp + F_i^{S||}, \quad (39)$$

where F_i^\perp stands for the force perpendicular to the reaction path,

$$F_i^\perp = -\nabla(R_i) + \nabla(R_i) \cdot \hat{t}_i, \quad (40)$$

and $F_i^{S||}$ is elastic force along the path \hat{t}_i :

$$F_i^{S||} = k(|R_{i+1} - R_i| - |R_i - R_{i-1}|)\hat{t}_i. \quad (41)$$

Here R_i is the position of configuration i , and k is elastic constant [40].

Maxima at the MEP correspond to the saddle points on the potential energy surface, and the highest energy corresponds to the potential barrier of reaction. In some cases, interpolation barriers may differ substantially from the exact values, which is caused by the small number of images in the vicinity of saddle point.

Climbing image NEB method (CI-NEB) allows high-accuracy determination of the saddle point energy [41]. After several iterations the highest energy configuration is determined, and the elastic force component is excluded from the eq. (39) for this particular image. Along with that, potential force component parallel to the path is added, resulting in:

$$F_i^{CI} = -\nabla(R_i) + 2\nabla(R_i) \cdot \hat{t}_i \hat{t}_i . \quad (42)$$

Thus, the image climbs up along the path and down perpendicular to the path. Other configurations here determine the particular degree of freedom for which the energy maximum is searched. Simultaneous optimization of all images allows using CI-NEB without any cost at computational efficiency with respect to original NEB.

2. INTERFACES OF NANOSIZED OBJECTS WITH MAGNETIC SUBSTRATES AS PROMISING SPIN FILTERING MATERIALS

The search for new spin filtering materials is one of the acute issues of modern spintronics. Conducting spin-polarized current, these materials may be implemented in magnetoresistive memory elements, hard disk scanning heads, and other devices. In many cases an insulating layer determines the main physical properties of the nanocomposites. Previously it was shown that planar hexagonal nanostructures such as graphene [42–45] and *h*-BN [43,46–48] have a great potential for utilization in spintronic devices due to the spin polarization induced by the contact with ferromagnetic substrate. We suppose that boron nitride and carbon nanotubes (BNNTs and CNTs) can also be used for this purpose.

Although the contact interaction of carbon and BN nanotubes with ferromagnetic substrates is supposed to be quite similar to that of the corresponding graphene and *h*-BN hexagonal monolayers, which can be considered as nanotubes of extremely large diameter, finite thickness of the tubes can result into significant change of interface properties. This effect is to be investigated in detail.

Interaction of graphene with transition metal surfaces is well studied by both theoretical and experimental methods [42–45]. The most stable configuration of mutual arrangement in graphene/Ni(111) composite were determined by means of density functional theory [43,44]. Three different possible positions of carbon atoms were considered (*top*, *hcp* and *fcc*) but new *bridge* configurations were found during the geometry optimization. The comparison of LDA and GGA-PBE approaches reveals that even though LDA describes such systems better than PBE functional, it tends to overestimate binding energies. Hence, using van-der-Waals

correction is necessary here [44]. Electronic exchange interaction with nickel lead to spin polarization of graphene even in presence of multilayer *h*-BN media [43].

According to previous studies [49–51], interaction between CNTs and metal substrate can vary from physical adsorption [49] to covalent bonding [50] depending on the metal species. It was found that there is a correlation between interaction energy and metal's work function [51]. It also influences charge transfer in these composites. Moreover, the Fermi-level shift of combined system with respect to pristine nanotube can be estimated with reasonable accuracy using phenomenological model developed by Hasegawa and Nishidate [49]. However, *3d* metal-based composites (e.g. Fe, Co, Ni) are more complicated due to their prominent magnetic and catalytic properties. Interface of (5,0) carbon nanotube with iron nanowire was studied by a combination of density functional theory (DFT) and Non-Equilibrium Green function (NEGF) method [52]. Carbon atoms bonded with iron were found to be slightly spin polarized. Minor spin polarization can be explained in terms of interface structure features. Nanowire is bumped into the tube [52] which leads to much smaller contact area in comparison with the tube lying on the metal slab [53]. Theoretical study of Fe-filled nanotubes deposited on Ni(111) and Cu(111) surfaces shows that the presence of Fe lead to significant change in nanotube's structure in both cases [54]. In fact, it turns to carbon “nanoarch” while metal surface becomes slightly corrugated. Charge density distribution confirms that both Fe and metal substrate affect C-C bonds leading to transformation of the tube.

The BN nanotubes are significantly more stable in terms of heat and chemical resistance [55] than CNTs. In contrast with CNTs, the BN nanotubes of a different chirality demonstrate the similar electronic structure which can be attributed to a wide band gap. It is reasonable to assume that BNNT's bonding with the metal surfaces may be quite similar to that of *h*-BN.

The perfect single-layer *h*-BN has been synthesized by CVD technique using some transition metals as supports [56]. The bonding of *h*-BN with ferromagnetic Co [46,48] and Ni [43,47] surfaces was found to be significantly stronger than that with other metals, such as Cu, Pd and Pt. This result is also confirmed by the theory and can be attributed to hybridization of *h*-BN π -states with 3*d* states of Ni [43,47]. Theoretical results [46,48] confirm the presence of covalent bonding between the *h*-BN and TM fragments in *h*-BN/Co(111) and *h*-BN/Co(0001) nanocomposites.

It was found that dispersion interaction plays an important role in bonding of *h*-BN with nickel while it's less important for cobalt since *h*-BN is likely to form covalent bonds with cobalt surface [46]. N atoms placed above the topmost metal sites were found to be much more favorable than B atoms. Boron atoms are then located either in *hcp* or *fcc* position. The study of composites' electronic structure reveals the presence of induced magnetic moment on the *h*-BN sheet. Nitrogen atoms possess magnetic moment parallel to that of metal atoms (positive spin polarization) while boron atoms have large magnetic moment being antiparallel to that of Co and Ni (negative spin polarization). However, the question of the curvature effect is still open, so the interaction between BNNTs and metal surfaces is to be investigated in detail.

Organic semiconductors are well-known as promising candidates for spintronics due to weak spin-orbit and hyperfine interaction [57–60]. Both giant magnetoresistance effect (GMR) and tunneling magnetoresistance (TMR) effect were observed in organic-based spin valves with rubrene, pentacene, tris(8-hydroxyquinolino)aluminum (Alq₃) and C₆₀ as spacers [59,61–66]. Fullerene C₆₀ is considered to be especially promising for use in organic electronics devices such as spin valves etc. [67–71] due to the absence of atoms other than carbon and, hence, weaker hyperfine interaction [66,72–74].

Films of C_{60} deposited on various noble and other closed-pack metal surfaces have been thoroughly studied both theoretically and experimentally [75–79]. Low-energy electron diffraction (LEED) analysis was found to be an efficient tool for defining structural parameters of interfaces [75,78]. These results are also supported by the density functional calculations. Formation of one or even several-atom vacancies due to the fullerene adsorption was reported in some cases [75,77,78,80] allowing tuning the interface properties by altering synthesis conditions. Recent studies of C_{60} films on Fe(001) surface reveal significant hybridization between fullerene π -states and iron 3d orbitals [81,82] leading to the change in charge and spin distribution in the contact area. Fullerene gets some degree of spin polarization opposite to that of the substrate. There are two different structures defined to be the most stable in this system being quite close to each other both in geometry of C_{60} /Fe(001) mutual arrangement and adsorption energy [80,82]. Thus, one can suppose the coexistence of these two and, probably, some more structures.

Half-metallic $La_{0.7}Sr_{0.3}MnO_3$ (LSMO) is widely used in spintronic devices due to its high spin polarization [63,72–74,83] even though it may vary due to the k broadening in direction perpendicular to the surface [84] resulting in reduction of spin polarization observed in experiment [85]. It has a lot of advantages comparing with conventional ferromagnetic materials (e.g. Fe, Co, Ni) being much less spin polarized and suffering from well-known conductivity mismatch problem. One way to solve this problem is to add tunnel barriers between FM electrodes and a spacer at the cost of increasing device complexity. Using half-metallic electrodes (LSMO) allows achieving up to the 95% contact spin polarization in MTJ devices without using any additional layers. Moreover, in contrast to abovementioned transition metals, LSMO is highly resistive against oxidation [57]. These features make LSMO an ideal candidate for using in spintronics. Detailed studies of magnetoresistance in LSMO/ C_{60} /Co vertical spin valve [60,72–74,83,86] including

effects of spacer thickness and surface morphology reveal very complex behavior combining GMR resulted from spin injection and TMR due to the presence of pinholes in organic spacer [73]. Magnetoresistance effect was found to increase drastically when C_{60} layer possesses higher crystallinity and larger grain size with many pinholes. Co then can diffuse through these pinholes reducing the effective thickness of spacer and causing tunneling rather than spin injection [73]. In contrast to that, samples with smoother C_{60} surface demonstrate completely different characteristics corresponding to the spin-polarized injection [73]. In order to prevent Co from diffusing into the pinholes, more complex LSMO/ C_{60} /AlO_x/Co devices were fabricated [72]. Aluminum oxide was found to suppress cobalt diffusion into the spacer layer effectively. Surprisingly, magnetoresistance effect changes its polarity in this case becoming positive instead of negative for original LSMO/ C_{60} /Co. This is explained in terms of competition between positive GMR channel and pinhole channel in latter case while positive MR dominating in former one [72]. Effect of Co/fullerene spinterface is also investigated both experimentally and theoretically by Liang et al. [83] However, the nature of interface between C_{60} and LSMO is relatively less investigated. Experimental study of its electronic structure by photoelectron spectroscopy was performed very recently [87]. Shift of HOMO and LUMO levels leading to n-p transition was observed when increasing the thickness of C_{60} . This was attributed to p-doping caused by oxygen diffusion from LSMO to the C_{60} layer.

Recently the composites of LSMO with carbon nanostructures such as graphene zig-zag nanoribbons and multiwall CNTs were studied by several scientific groups [88–92]. La_{0.8}Sr_{0.2}MnO₃ nanoparticle-decorated carbon nanotubes demonstrate metal-insulator transition and paramagnetic to superparamagnetic phase transition both rising from LSMO nanoparticles presence [88]. Anisotropic nature of magnetic field-magnetization curve and high coercivity allows using carbon nanotubes fabricated on the La_{0.66}Sr_{0.33}MnO₃ by dip deposition method in

spintronic device applications [89]. Another application of LSMO/CNT composites is electrocatalysis due to K. Miyazaki's research [90]. LSMO/CNT composites were found to be promising as cathode catalysts for oxygen reduction.

It was found that exchange interaction with LSMO support causes the high rate spin polarization of graphene zig-zag nanoribbons, whereas carbon nanotubes remain to be slightly spin-polarized. Devices of multiwall carbon nanotube between two half-metallic LSMO electrodes demonstrate electric conductance increasing at lower temperatures [91] along with high spin polarization of electrodes and the resistance for spin injection [92]. The experimental results were supported by density functional theory calculations.

The special kind of magnetic ordering in C_{60} molecule rising from the interaction with manganese atoms was proposed to be responsible for binding between fullerene and LSMO and complex magnetic exchange interaction. This encourages one to suppose that binding with manganese should affect electronic structure of carbon nanotubes deposited on LSMO surface as well. Interfaces of CNTs with ferromagnetic substrates are supposed to demonstrate significant spin polarization due to the interaction with 3d metals. One could expect even higher values of spin polarization for CNT when interacting with half-metallic material.

The present study is to characterize the interactions of buckminsterfullerene C_{60} , CNTs or BNNTs with ferromagnetic transition metals, namely, Fe, Co and Ni, as well as half-metallic $La_{0.7}Sr_{0.3}MnO_3$, and to elucidate the nature of spin polarization of the nanosized fragments caused by interactions with ferromagnetic supports, particularly, to reveal if the 3d metal atoms are in charge of the composite properties in LSMO case.

3. Computational methods

3.1 Study of NT interfaces with transition metal surfaces

The first-principles density functional theory calculations of nickel and cobalt interfaces with BN and carbon nanotubes were performed using VASP code [93–96]. Local Density Approximation (LDA) [5], plane wave basis set and ultrasoft Vanderbilt-type pseudopotentials [28,97] were implemented for interfaces with zigzag nanotubes while GGA PBE potential [98,99] along with projector augmented wave [29,100] method (PAW) and D3 Grimme's correction [8] of weak dispersion interaction were used when studying armchair nanotubes. The energy cut-off was specified as 400 eV in all calculations.

First, unit cells of bulk Co and Ni were optimized. Then they were cut normal to [001] and [111] crystallographic directions in order to obtain corresponding surfaces. Next, metal slabs were simulated by constructing supercells containing several surface unit cells along one of the directions. The length of slabs (16.85 Å for Co and 16.90 for Ni) was sufficient for armchair tubes in neighboring images could be placed distant from each other in order to simulate isolated nanotubes on metal surface. Translation vector being parallel to the metal surface and normal to the tube axis was fixed at the values of 17.11 and 19.26 Å for Ni and Co, respectively, when studying interfaces with zigzag nanotubes. These models were chosen with respect to the symmetry and cell matching.

To reproduce the main features of the electronic structure and spin states of the *NT/TM* composites, 8 layers of Co and 9 layers of Ni were chosen to design slab models. Artificial interactions in periodic boundary conditions were avoided by setting the vacuum interval of approximately 10 Å in direction normal to the interface.

Then, nanotubes optimized structures were deposited on metal surfaces in the way ensuring the best commensuration between slab's and tube's translation vectors. Metallic (9,0) and semiconducting (10,0) carbon nanotubes as well as (9,0)

BN nanotube were used to describe zigzag nanotubes' performance, and (5,5) carbon and BN nanotubes with almost the same diameter (6,97 and 7,05 Å, respectively)) were used for armchair nanotubes' interfaces description.

The Mönkhorst-Pack [101] k -point Brillouin sampling was used. The k -point grid contained 6 points along the least translation vector and 1 point along two large translation vector for NT(n,0)/TM interfaces. For the case of armchair NT(5,5)/TM composites, k -point grid contained 12 points along the least translation vector and 1 point along the largest translation vector. Hexagonal symmetry of Co(0001) supercell was taken into account by specifying number of k -points in larger lateral direction as 2. This is reasonable because a vector there is defined not only by the first coordinate but has also a small contribution of the second one. For Ni(111), orthorhombic supercell was used, so 1 k -point was enough in this case. All abovementioned values were carefully tested and found to be sufficient in describing such interfaces.

To reveal the stability of interfaces, the binding energy was estimated using following equation:

$$E_b = E_{t(NT/TM \text{ slab})} - E_{t(NT)} - E_{t(TM \text{ slab})}, \quad (43)$$

where E_b is binding energy of a nanotube with metal slab surface, $E_{t(NT/TM \text{ slab})}$ is the total energy of hybrid structure, $E_{t(NT)}$ is nanotube's total energy, and $E_{t(TM \text{ slab})}$ is the total energy of a metal slab. The magnitude of spin polarization was calculated as:

$$\xi = \frac{n_{\uparrow} - n_{\downarrow}}{n_{\uparrow} + n_{\downarrow}}, \quad (44)$$

where n_{\uparrow} and n_{\downarrow} are electron densities at the Fermi level for spin-up and spin-down states, respectively.

3.2 Study of C₆₀/Fe(001) nanocomposite

The first-principles density functional theory calculations of C₆₀/Fe(100) composites were performed using VASP code [93–96]. GGA PBE potential [98,99] and projector augmented wave [29,100] method (PAW) were implemented. Geometry optimization was performed until the forces acting on atoms were less than 0.01 eV/Å.

First, unit cell of bulk Fe was optimized. Then Fe(100) surface was constructed by cutting it along the corresponding crystallographic plane. In order to simulate C₆₀/Fe(100) composites, we used 4×4 supercell of iron surface. This means that distance between the carbon cages of two neighboring fullerenes (~4.34 Å) is considerably close to that of the solid fullerene (3.13 Å) [102]. Setting the smaller iron substrate is not reasonable since the distance between C₆₀ molecules would be less than that of the solid C₆₀. This, in turn, would lead to the overbinding between neighboring molecules which, in fact, should be bonded via weak van-der-Waals forces. Since the interaction between iron surface and C₆₀ is supposed to involve strong chemical bonding and charge redistribution [80–82], we then consider van-der-Waals supply to be negligible and do not use any correction for it. Artificial interactions in periodic boundary conditions were avoided by setting the vacuum interval of approximately 12 Å in direction normal to the interface. Preliminary tests showed that 8 atomic layers are enough for sufficient representing the features of iron slab.

As previously, the Monkhorst-Pack [101] k-point Briloin sampling was used. The k-point grid contained 3×3×1 points along a, b and c directions, respectively. The energy cut-off was specified as 400 eV in all calculations.

Energy of bonding between fullerene and Fe(100) slab was estimated as:

$$E_b = E_c - E_f - E_{Me}, \quad (45)$$

where E_c , E_f and E_{Me} are total energies of composite, fullerene and metal slab, respectively.

Deformation energy of fullerene and iron was found as:

$$E_d = E_{comp} - E_{pristine}, \quad (46)$$

where E_{comp} and $E_{pristine}$ correspond to the energy of iron (fullerene) in the composite and the energy of its pristine optimized structure.

3.3 Study of LSMO-based nanocomposites

The first-principles density functional theory calculations of LSMO/C₆₀ and LSMO/CNT composites were performed using VASP code [93–96]. GGA PBE potential [98,99] with taking into account Hubbard corrections (GGA+U) [19,103] and projector augmented wave [30,104] method (PAW) were implemented. D3 Grimme correction of weak dispersion interactions [17] was used in order to describe the interaction between nanotubes and LSMO substrate correctly. The U=2 and J=0.7 eV parameters of GGA+U approach are adopted from earlier calculations of LSMO [105–107]. Geometry optimization was performed until the forces acting on atoms were less than 0.01 eV/Å. The energy cut-off was specified as 450 eV in all calculations.

First, unit cell of bulk LSMO was optimized, and the *a* translation vector is found to be equal to 3.886 Å which is in a good agreement with experimental data (*a*=3.876 Å [108] and *a*=3.87 Å [109]) and previous theoretical calculations (*a*=3.89 Å [105]). Then, LSMO(001) surface was constructed by cutting it along the corresponding crystallographic plane. Depending on the synthesis conditions the slab of LSMO can be terminated by either Sr-O or Mn-O layer. Mn-O terminated surface was chosen for calculation of interface with C₆₀ since it was investigated in experimental works [72–74]. 4×4×1 supercell of LSMO surface which means that, in periodic boundary conditions, fullerene molecules are distant from each other (distance between them is ~8.6 Å) and can be considered as isolated. Lattice vectors were then set to be *a*=*b*=15.544 Å, *c*=30.000 Å. Both

possible terminations were considered for nanotubes' interfaces in order to prove the crucial role of interaction with transition metal atom so one can expect much stronger interaction with Mn-O terminated surface and only a weak van-der-Waals interaction with Sr-O terminated one.

Two different supercells of LSMO slab were used: $8 \times 1 \times 1$ ($a=31.09$ Å, $b=3.88$ Å, $c=30.00$ Å) for CNT(9,0) and $6 \times 2 \times 1$ ($a=23.32$ Å, $b=7.77$ Å, $c=30.00$ Å) for CNT(5,5). However, CNT(9,0) was still contracted by ~9% and CNT(5,5) was stretched by ~5% which changes their properties significantly. Neighbouring nanotubes must be located as far as possible from each other, so LSMO slabs consisted of 8 and 6 unit cells in direction normal to the tube's axis, which were maximum values for providing both correct description and computational efficiency. We suppose that mainly the topmost layer should be responsible for the interface properties so one can use an oversimplified model of 1 unit cell along c direction without any cost at computational accuracy while considerably increasing the speed of calculation. Artificial interactions in periodic boundary conditions were avoided by setting the vacuum interval of approximately 10 Å in direction normal to the interface.

The Mönkhorst-Pack [101] k-point Brillobin sampling was used. The k-point grid contained $2 \times 2 \times 1$ points along a , b and c directions, respectively, for LSMO/C₆₀ nanocomposites, $1 \times 6 \times 1$ and $1 \times 2 \times 1$ points along a , b and c directions for different nanotubes' supercells.

Energy of bonding between nanosized fragments and LSMO slab was estimated as:

$$E_b = E_c - E_{NS} - E_{LSMO}, \quad (47)$$

where E_c , E_{NS} and E_{LSMO} are total energies of composite, nanostructure and LSMO slab, respectively. Charge and magnetic moment on fullerene molecule and carbon nanotubes were estimated according to the Bader charge analysis [110–112].

4. RESULTS AND DISCUSSION

4.1 Interaction between carbon and boron nitride nanotubes and ferromagnetic Co(0001) and Ni(111) substrates

In this work the following possible configurations of *NT/TM* composite slabs were considered: *top:fcc* and *top:hcp* for CNTs (carbon atoms are placed under *top*, *hcp* and *fcc* positions of the TM substrates) and *top(N):fcc(B)*, *top(N):hcp(B)*, hereafter *top:fcc*, *top:hcp*, for BNNTs (the nitrogen atoms are placed under *top* and boron atoms are placed under *hcp* or *fcc* positions of the substrate, see Figure 1). It was found that *top(B):fcc(N)* and *top(B):hcp(N)* configurations are approximately 1.5 eV higher in energy than *top(N):fcc(B)* and *top(N):hcp(B)* ones, in agreement with the data obtained for *h*-BN monolayer [42,43,48].

Table 1 shows the binding energies of *NT(n,0)/TM* composites as well as corresponding bond distances. All Co-based nanocomposites were found to be substantially more energetically favorable than Ni ones. The CNT(9,0)(*top:hcp*)/Co, CNT(9,0)(*top:fcc*)/Ni, CNT(10,0)(*top:fcc*)/Co, CNT(10,0)(*top:hcp*)/Ni, BNNT(9,0)(*top:hcp*)/Co and BNNT(9,0)(*top:fcc*)/Ni nanocomposites were found to be more energetically favorable than others. The CNT(9,0)/TM interfaces demonstrate slightly stronger bonding than CNT(10,0)/TM ones, which can be attributed to the difference in their conducting properties. Bond distances in *top:fcc* and *top:hcp* configurations remain virtually the same (the difference ≤ 0.01 Å). A slight displacement of the nanotube's atoms from the *top* sites was observed for CNT(9,0)(*top:fcc*)/Co, CNT(9,0)(*top:hcp*)/Co, CNT(9,0)(*top:fcc*)/Ni, CNT(10,0)(*top:hcp*)/Ni and BNNT(9,0)(*top:hcp*)/Ni configurations. The angles between TM-X bonds (X=N, C) and normal to TM surface are in the range of 5-6°. Similar phenomena was also found at graphene monolayer/Ni(111) interface [44].

The *top:fcc* configuration of CNT(5,5)/Co and *top:hcp* configuration of CNT(5,5)/Ni relaxed into the *bond* configuration (carbon bond is placed above the TM atom) during the optimization (Figure 2). The deformation of the tube was observed in these cases (see Figure 7). This new configuration may be referred to the *bridge* configurations found in graphene/Ni(111) composite [44]. It should be noticed that only a slight displacement of the tube's atoms from *top* sites was observed in interfaces of Co and Ni with zigzag nanotubes [53]. However, *bond* configuration is not stable for BN nanotubes, initial structure relaxing into one of the favorable configurations. For both Ni and Co-based composites the energy difference between configurations is negligible (see Table 2), the biggest one observed in CNT(5,5)/Ni system (~ 0.15 eV) is still too small to separate them in synthesis condition. In general, bonding of TM slab with carbon nanotubes is stronger than that with BNNTs, in agreement with previous studies [53]. In contrast to planar structures and zigzag nanotubes, Ni-based composites are more energetically favorable than Co-based ones.

Table 1. The binding energies and bond distances for $NT(n,0)/TM$ slabs

Nanotube	Metal	<i>top:fcc</i>		<i>top:hcp</i>	
		E_b , eV	z , Å	E_b , eV	z , Å
CNT(9,0)	Co	-4.646	1.939	-4.720	1.944
	Ni	-2.600	1.922	-2.374	1.929
CNT(10,0)	Co	-4.523	1.944	-4.360	1.949
	Ni	-2.260	1.921	-2.311	1.931
BNNT(9,0)	Co	-3.876	1.993	-3.926	1.990
	Ni	-1.891	1.968	-1.693	1.967

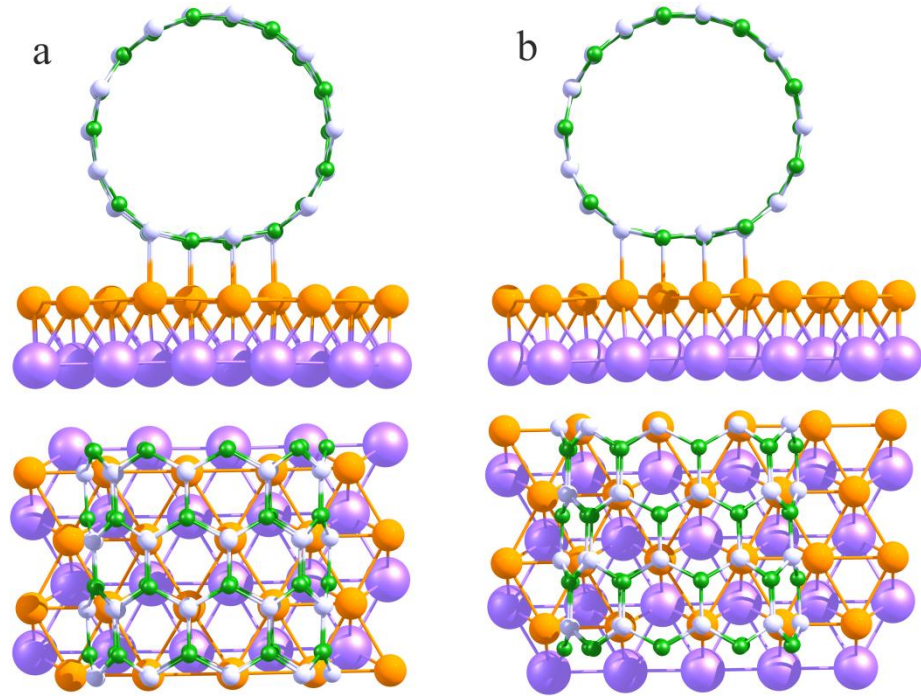


Figure 1. (a) $top(N):hcp(B)$; (b) $top(N):fcc(B)$ configurations of BNNT(9,0)/Co nanocomposite. Boron/nitrogen atoms are represented as green and gray balls, respectively. Orange and blue balls correspond to the first and second atomic layers of nickel atoms, respectively

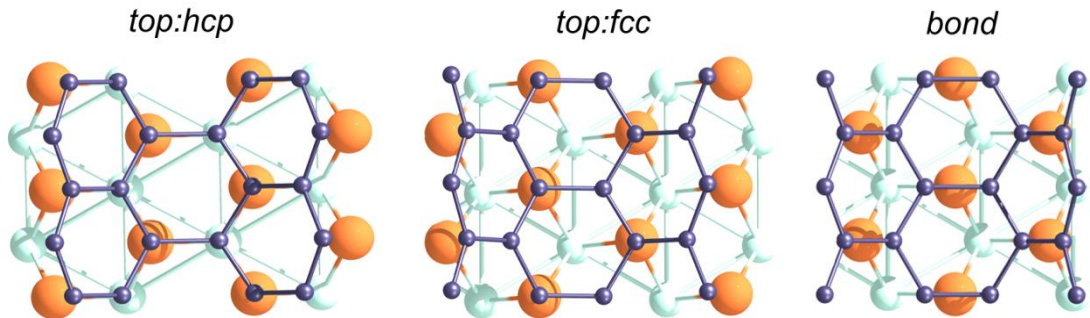


Figure 2. Configurations of armchair nanotubes' location on the metal substrate. Carbon atoms presented as small dark balls; big orange and smaller light green balls correspond to metal atoms of first and second layer, respectively. Upper part of the tube is not presented for the sake of better representation.

Table 2. The binding energies and bond distances for *NT/TM slabs*

Nanotube	Metal	<i>top:fcc</i>		<i>top:hcp</i>		<i>Bond</i>	
		E_b , eV	z , Å	E_b , eV	z , Å	E_b , eV	z , Å
CNT(5,5)	Co	—	—	-1.534	2.040	-1.515	2.044
	Ni	-1.918	2.030	—	—	-2.074	2.033
BNNT(5,5)	Co	-1.097	2.097	-1.150	2.099	—	—
	Ni	-1.675	2.055	-1.680	2.063	—	—

Then, the electronic structure of composites was analyzed. Carbon partial density of states (PDOS) of CNT(n,0)/Ni and CNT(n,0)/Co nanocomposites for carbon atoms in direct contact with the metal surfaces as well as at the opposite side of the nanotubes are presented in Figures 3a, 3b. The nitrogen and boron PDOSes of BNNT(9,0)/Co composite are presented in Figure 4.

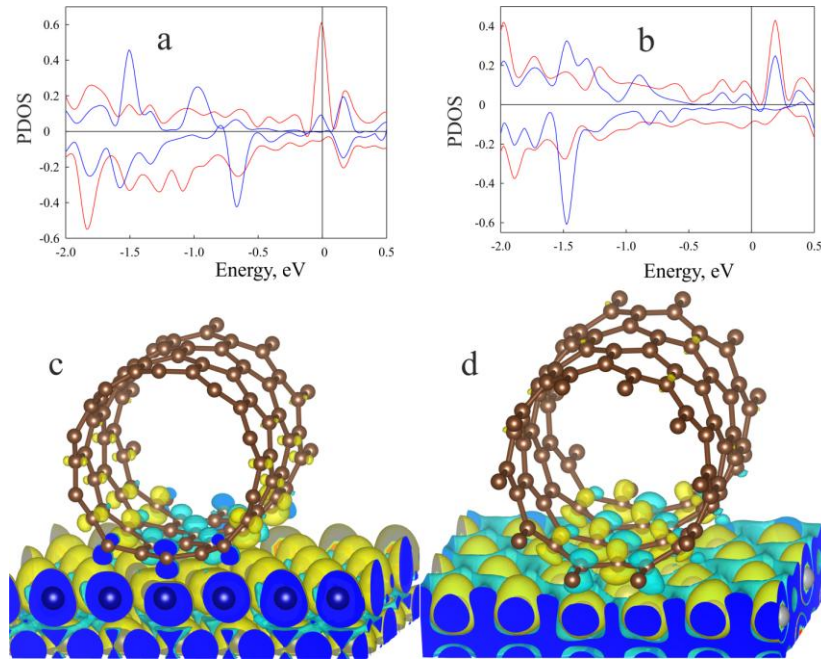


Figure 3. (a) Partial density of states (PDOS) of CNT(10,0)/Co carbon atoms. (b) Partial density of states of CNT(10,0)/Ni carbon atoms. (c) Spatial distribution of spin density in CNT(10,0)/Co. (d) Spatial distribution of spin density in CNT(10,0)/Ni. Red (blue) line corresponds to the PDOSes of the atoms near to (far

from) interfaces (a,b). Yellow (blue) color corresponds to spin-up (spin-down) electron density (c,d)

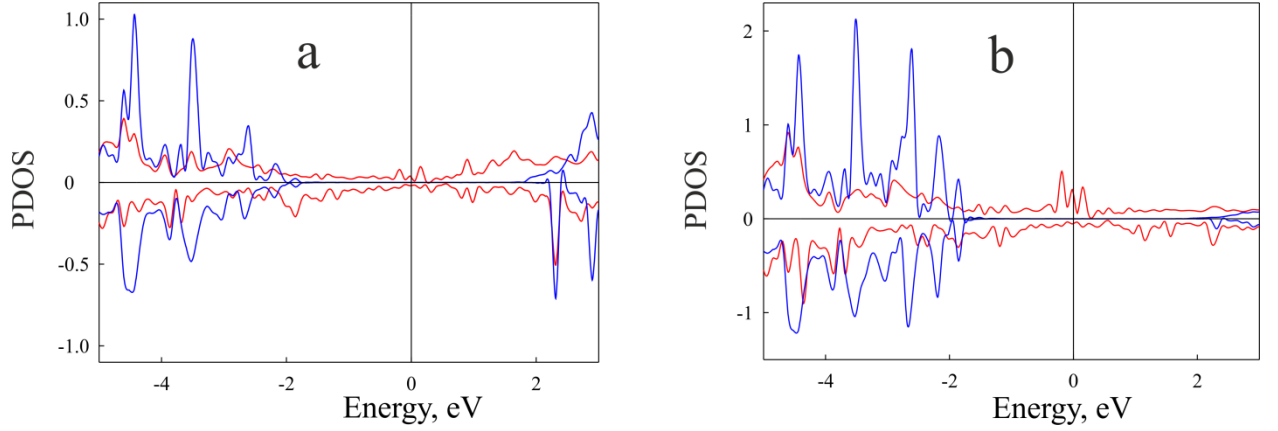


Figure 4. Boron (a) and nitrogen (b) PDOSes of BNNT(9,0)/Co composite. Red (blue) line corresponds to atoms near to (far from) the interface.

Interfaces of different CNTs with the same type of substrate display very similar state distribution near the Fermi level. In particular, atoms in the direct contact with the metal surfaces demonstrate significant differences between spin-up and spin-down density of states. However, atoms far from the interface are not spin-polarized.

In the case of CNT(10,0)(*top:fcc*)/Co composite, a visible negative spin polarization of the *top* atoms and weak positive spin polarization of atoms far from the interface is detected (Figure 3c) with no spin polarization observed at *fcc* carbon atoms. In contrast, for CNT(10,0)(*top:hcp*)/Ni a positive spin polarization of *hcp* atoms (Figure 3d) as well as the *top* atoms negative spin polarization was detected.

In contrast with CNTs, the electronic structure of the BNNT's atoms distant from the interface is quite similar to that of an isolated nanotube with band gap approximately equal to 3.8 eV. This effect can be explained in terms of strong localization of electrons in BN nanotube, which leads to the difficulties in spin

polarization spreading along the tube's diameter. However, contact-induced polarization leads to the filling of the unoccupied states and vanishing of the band gap. It causes an appearance of local conductivity in BNNT(9,0)/Ni and BNNT(9,0)/Co composites. According to the spin density spatial distribution (Figure 5), the nitrogen atoms of BNNT/Ni are positively spin polarized, while only weak negative polarization is observed at boron atoms. In contrast, significantly stronger negative polarization on B is observed in the case of BNNT/Co due to the much shorter distance between boron and cobalt atoms in *top:hcp* configuration than between B and Ni in *top:fcc* (3.749 and 5.761 Å, respectively).

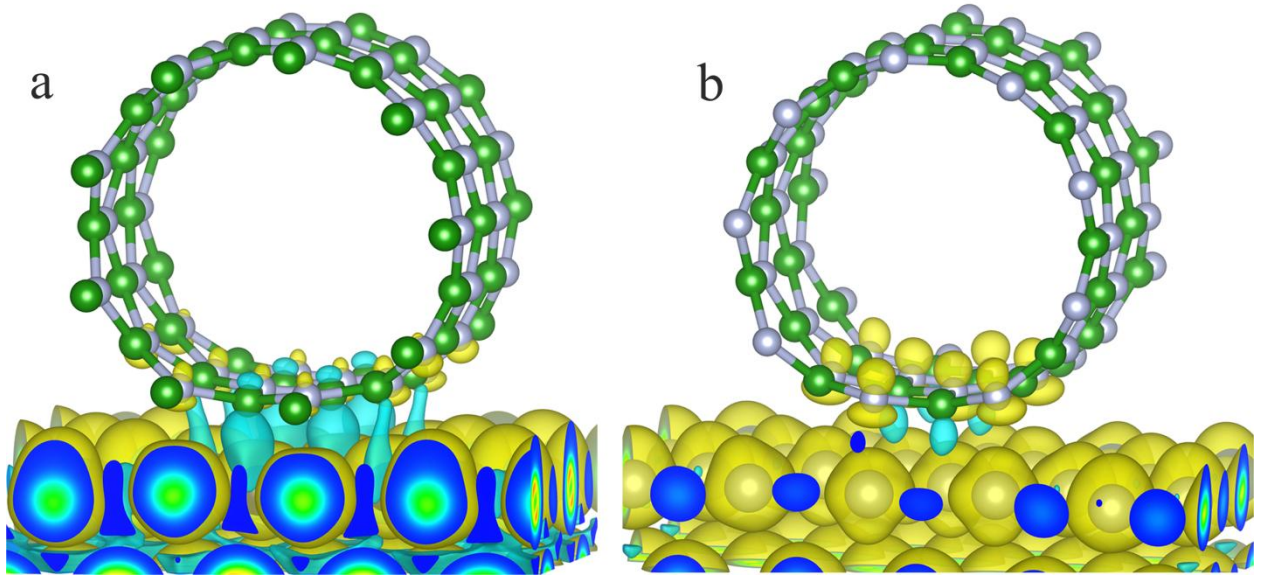


Figure 5. Spin density spatial distribution of BNNT(9,0)/Co (a) and BNNT(9,0)/Ni (b). Yellow (blue) color corresponds to spin-up (spin-down) electron density. Boron (nitrogen) atoms are represented as green (gray) balls

The magnitude of nanotubes' total spin polarization is presented in Table 3. The NTs deposited on Co surface are significantly more spin polarized than those on Ni slabs. This can be attributed to the different number of electrons for these ferromagnetic metals. Conducting nature of CNT(9,0) results in spreading of both

spin-up and spin-down density along the tube's diameter and decreasing of spin polarization value.

Table 3. Magnitude of spin polarization of nanotube's atoms for the most energetically favorable *NT/TM* configurations

ξ , %		
Nanotube	Co	Ni
CNT(9,0)	35	14
CNT(10,0)	87	17
BNNT(9,0)	55	13

According to the partial densities of states plotted for the armchair nanotube atoms being in direct contact with metal surface and for the atoms on the opposite side of the tube (Figure 6), BN (5,5) nanotube demonstrates local contact-induced conductivity while the rest of the tube remains to be an insulator, as well as the (9,0) one [53].

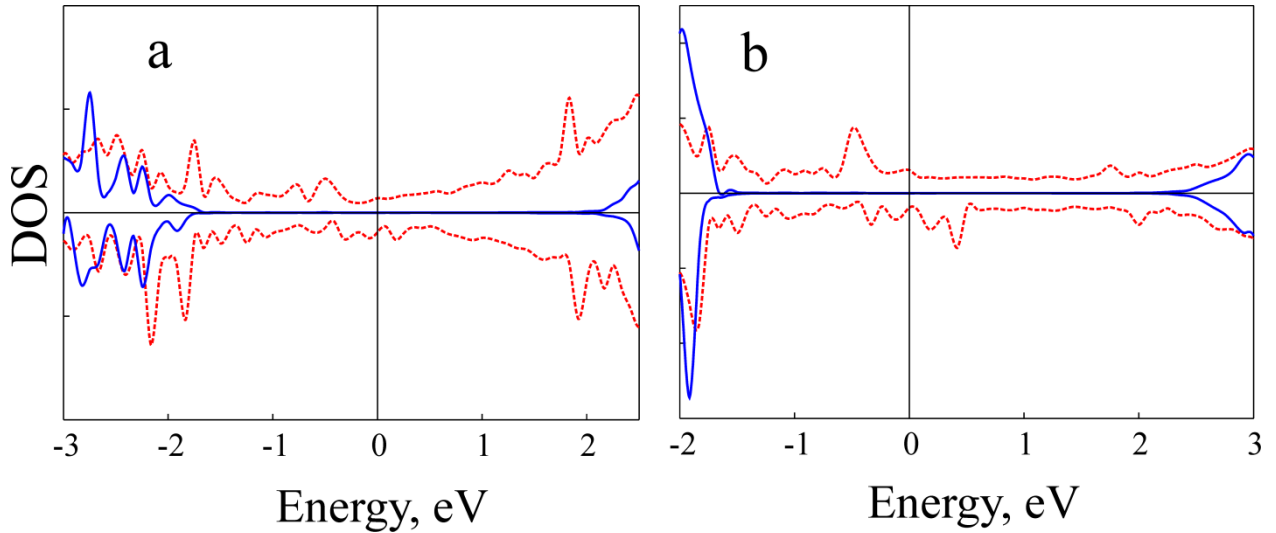


Figure 6. Boron (a) and nitrogen (b) PDOSes of BNNT(5,5)/Ni composite. Red (blue) line corresponds to atoms near to (far from) the interface.

The positive spin polarization was observed for the nitrogen atoms while the boron atoms are negatively spin-polarized (Figure 7b, 7d). Spin density distribution is quite similar for all 4 BNNT-based nanocomposites. However, their magnitude of spin polarization differs significantly (see Table 4).

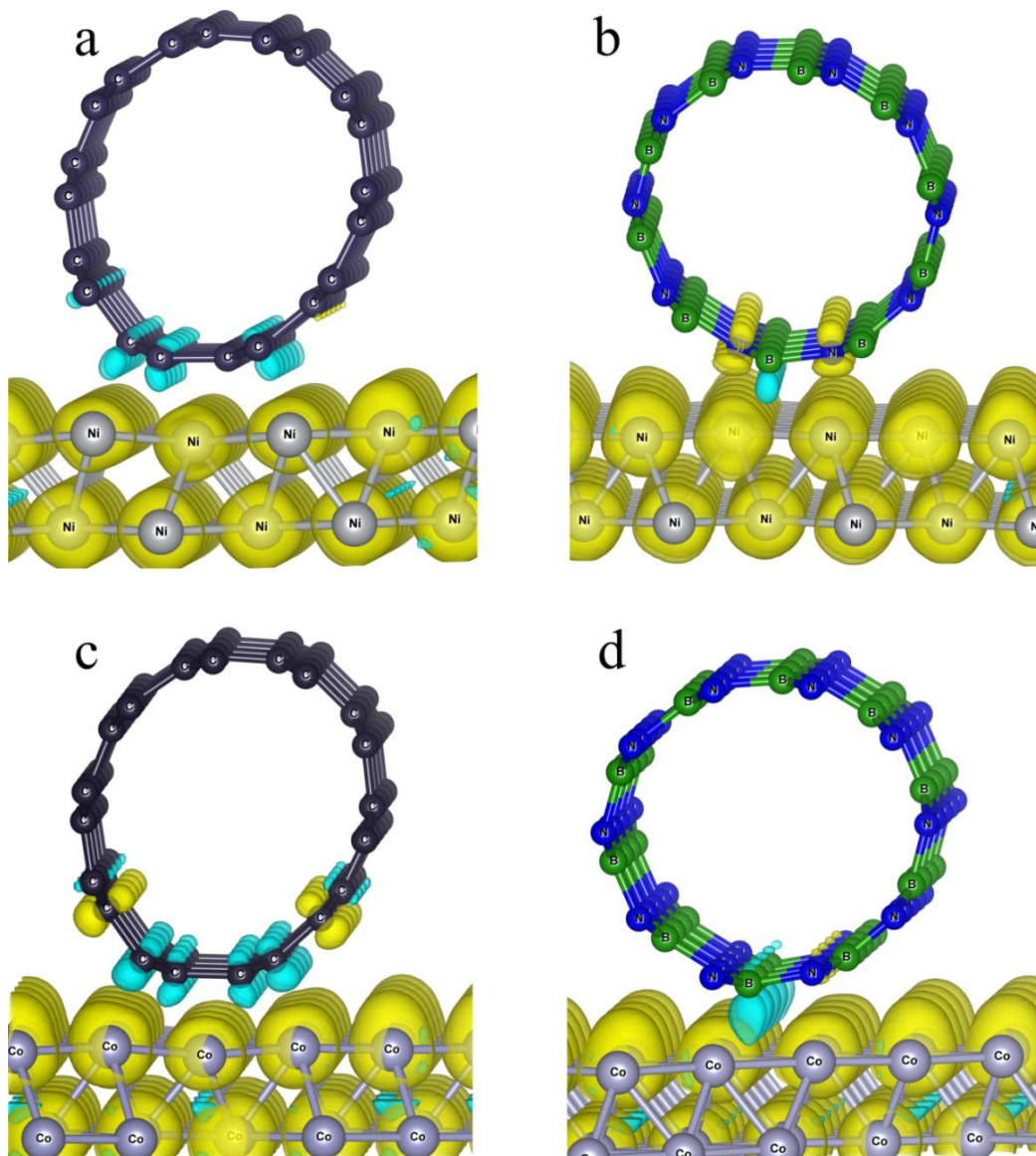


Figure 7. Spatial distribution of spin density in (a)CNT(5,5)/Ni; (b) BNNT(5,5)/Ni; (c) CNT(5,5)/Co; (d) BNNT(5,5)/Co.

Yellow (blue) color corresponds to spin-up (spin-down) electron density

This can be attributed to the larger distance between boron and metal atoms in *top:fcc* configuration which weakens the effect of its polarization. Indeed, we can see that polarization of nanotube BNNT(5,5)/Co (*top:hcp*) system is mainly caused by negative polarization of boron atom while it's almost fully compensated by positively polarized nitrogen atoms (see Figure 7) in BNNT(5,5)/Co (*top:fcc*). The same tendency, though less pronounced, can be observed in BNNT(5,5)/Ni composites (see Table 4). These results are in good agreement with those for planar *h*-BN sheet [46] and (9,0) BN nanotubes [53].

Table 4. Magnitude of spin polarization of nanotube's atoms at the Fermi level

Nanocomposite	ξ , %
BNNT(5,5)/Co (<i>top:fcc</i>)	1.5
BNNT(5,5)/Co (<i>top:hcp</i>)	15.2
BNNT(5,5)/Ni (<i>top:fcc</i>)	11.7
BNNT(5,5)/Ni (<i>top:hcp</i>)	24.8
CNT(5,5)/Co (<i>bond</i>)	13.0
CNT(5,5)/Co (<i>top:hcp</i>)	8.8
CNT(5,5)/Ni (<i>bond</i>)	3.9
CNT(5,5)/Ni (<i>top:fcc</i>)	17.4

Electronic structure of carbon atoms being distant from interface is also quite similar to that of an isolated nanotube, while the vanishing of the gap is observed for atoms in direct contact with metal slab (Figure 8). These atoms are visibly negative spin-polarized (Fig. 7a, 7c). There is also a positive polarization of the next atoms in CNT(5,5)/Co (*bond*). However, we can see again that both for Co and Ni-based interfaces ξ depends strongly on the configuration (Table 4) while energy difference between them is very small. This means that the yield of both configurations in synthesis would be almost the same which, in turn, makes their

utilization in spintronic devices much less perspective even though some of them show significant values of spin polarization.

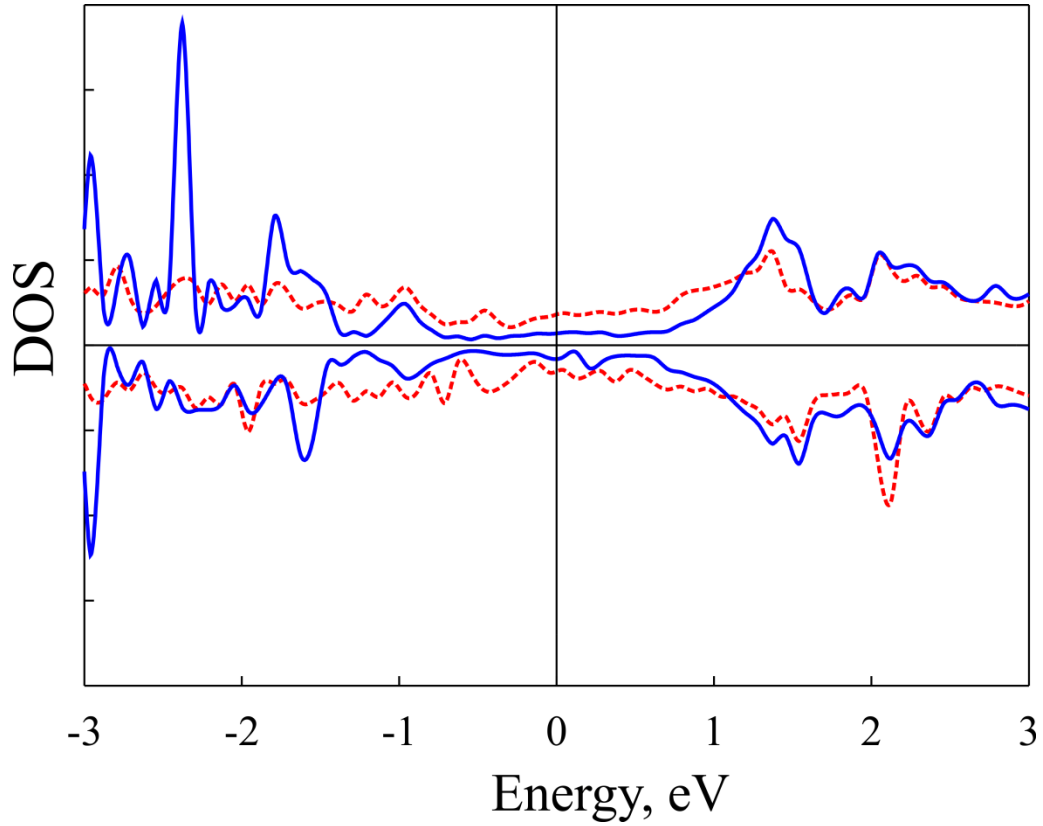


Figure 8. Partial density of states of CNT(5,5)/Ni carbon atoms. Red (blue) line corresponds to atoms near to (far from) the interface.

4.2 Buckminsterfullerene C_{60} interfaces with Fe(001) surface

Six different possible high-symmetry configurations of C_{60} deposition on the Fe(100) surface were considered as initial structures (see Figure 9): four ones with carbon hexagon, pentagon, hexagon-hexagon bond or hexagon-pentagon bond placed upon the iron atom, and two ones with 2 or 4 carbon atoms belonging to one hexagon placed directly or nearly upon corresponding 2 or 4 iron atoms. However, most of them then relaxed to one of the following configurations with much lower symmetry: bridge-1 and bridge-2 have the only difference in the degree of metal

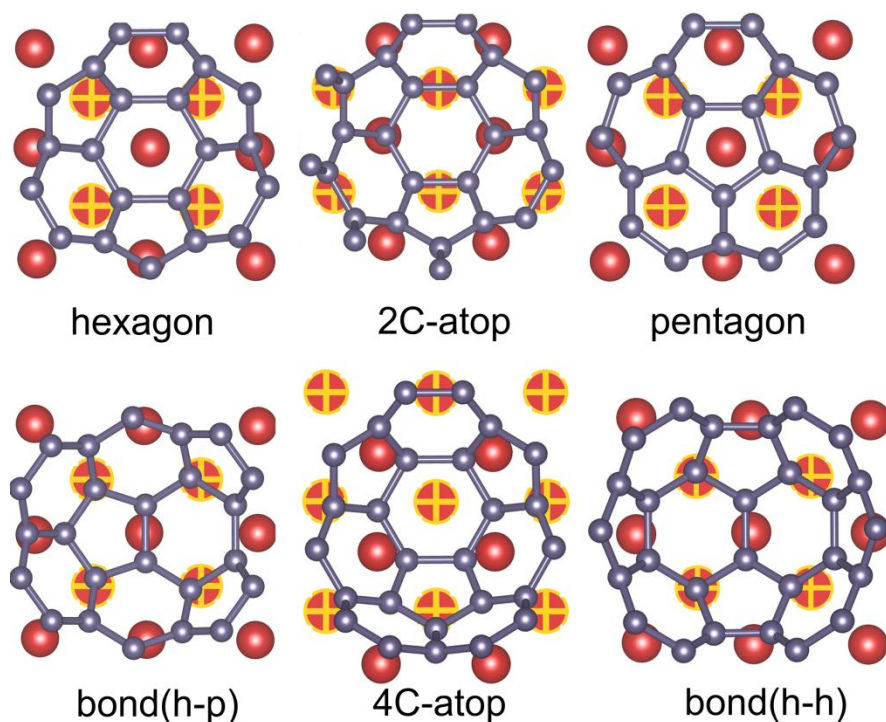


Figure 9. Initial geometries of $C_{60}/Fe(001)$ interfaces. Carbon atoms are denoted as grey balls, red and yellow-red ones correspond to the first and second layer of iron surface. For the sake of better clarity, only the bottom part of fullerene is presented.

slab deformation while the orientation of C_{60} is virtually the same (Figure 10); initial 2C-atop structure is slightly distorted due to the carbon atoms displacement from top positions resulted in 2 corresponding carbon bonds placed upon Fe atoms (see Figure 10), and hereafter denoted as 2C-bond; the most symmetric 4C-atop configuration was however the least favorable among all (see Table 5). 2C-bond and 4C-atop structures have almost the same binding energies which is expectable due to their similarity. Much larger energy difference between bridge-1 and bridge-2 may be explained in terms of the deformation energy of iron slab. Indeed, the slab is substantially more distorted in former case which is also confirmed by the value of deformation energy which is by 0.18 eV higher than that of bridge-2

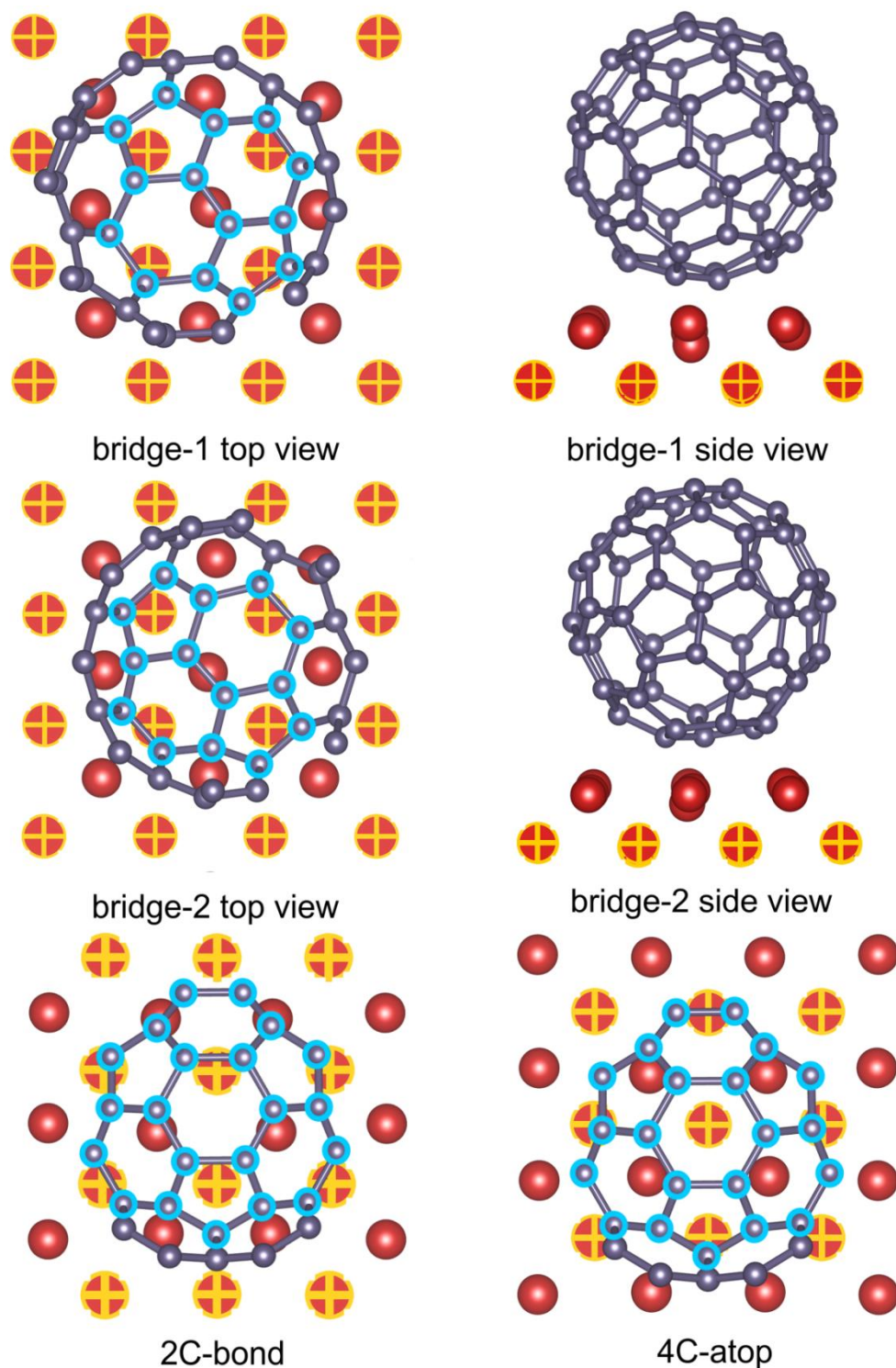


Figure 10. Geometries of optimized $C_{60}/Fe(001)$ structures. Carbon atoms are denoted as grey balls, red and yellow-red ones correspond to the first and second layer of iron surface. Contacting C_{60} atoms are denoted by blue circles. For the sake of better clarity, only the bottom part of fullerene is presented.

(0.482 and 0.305 eV for bridge-1 and bridge-2, respectively) while difference in binding energy is equal to 0.19 eV. Values of binding energy themselves are high (~3 eV) which confirms the presence of chemical bonding in the system, in agreement with previous theoretical and experimental data [80–82]. Both bridge-1 and bridge-2 configurations are somewhat similar to the ones reported in literature [80,82] in terms of fullerene's orientation confirming our suggestions about high movability of C₆₀ on iron surface.

Table 5. Values of binding energy, charge, magnetic moment and Fermi-level spin polarization in Fe(100)/C₆₀ composites

Configuration	Binding energy, eV	Total C ₆₀ charge, e	Charge on contacting C ₆₀ atoms, e (divided by total charge, %)	Magnetic moment of C ₆₀ molecule, μ_B	Spin polarization at Fermi level, %
bridge-1	-3.082	2.217	2.086 (94.0)	-0.124	-72.6
bridge-2	-3.274	2.112	2.017 (95.5)	-0.153	38.3
2C-bond	-2.945	1.904	1.554 (86.7)	-0.040	-28.2
4C-atop	-2.921	1.667	1.445 (81.6)	-0.153	51.7

For each configuration, charge and spin distribution were estimated using Bader charge analysis [110–112] with high-density FFT grid (see Table 5). We found magnetic moments to be slightly lower and charge of C₆₀ molecule to be slightly higher than that reported in literature [82]. This can be attributed to the difference of composite's configurations or to the different density of FFT grid and

does not change overall conclusions. Value of spin polarization at Fermi level was calculated according to the equation (2).

The analysis of partial densities of states (PDOS) shows that electronic structure of C_{60} on the Fe(001) surface is strongly distorted comparing with that of the bare fullerene (see Figure 11). Band gap is vanishing, and peaks are shifted to the lower energies which confirm the major deformation of fullerene playing a key role in composite formation [82].

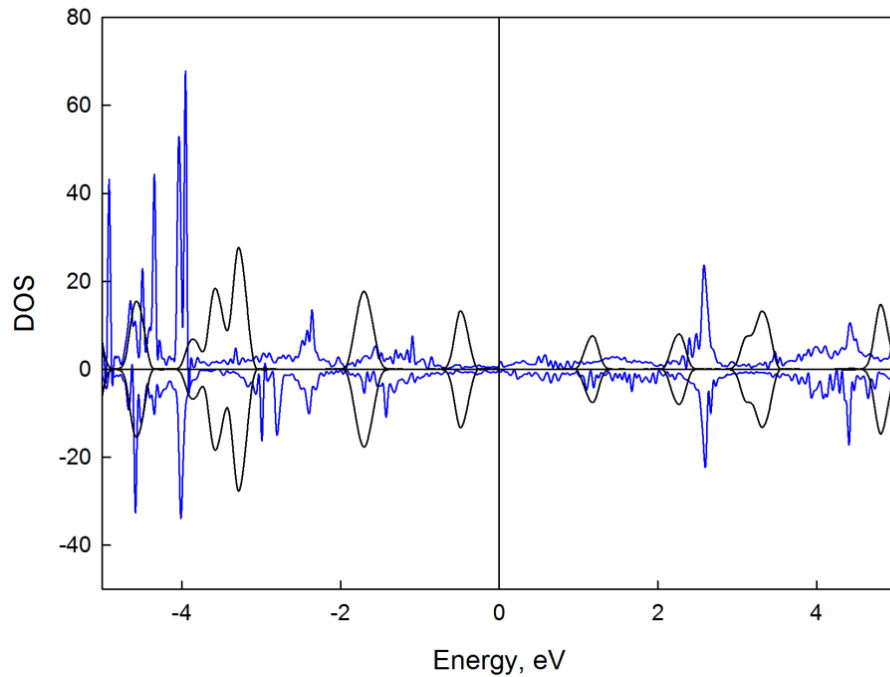


Figure 11. PDOS of C_{60} molecule for bridge-2 configuration of $C_{60}/Fe(001)$ composite (blue line) in comparison with DOS for pristine fullerene (black line)

It should be emphasized that PDOS remains its features both for the atoms being in direct contact with substrate and for the opposite side atoms (Figure 12). This trend is observed in all four structures we considered. In order to shed the light on the spin density distribution in $C_{60}/Fe(100)$ composites, we present its spatial patterns for each configuration (see Figure 14). Carbon atoms are negatively spin polarized, and the more is the overlapping between carbon and iron

the less is the negative spin density on carbon atom, in perfect agreement with data previously reported [82].

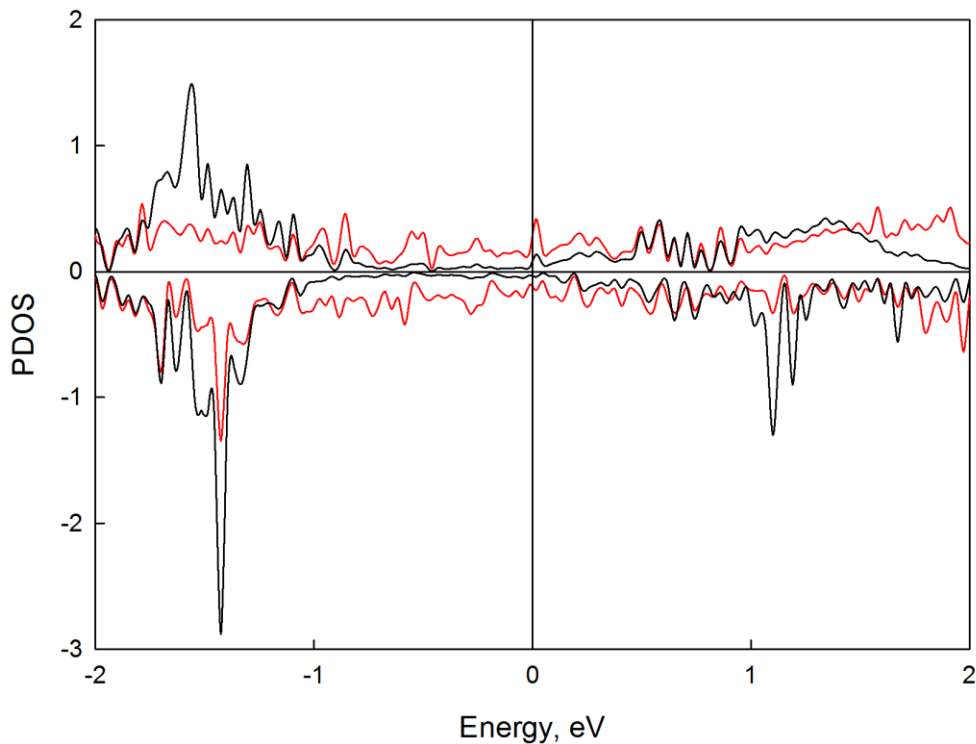


Figure 12. PDOS of fullerene atoms being in direct contact with iron slab (red line) and atoms from the top part of the fullerene (black line)

Along with that, total charge on fullerene's molecule is also distributed unequally (see Table 5). We analyzed charges on atoms contacting with iron substrate (14 atoms for bridge-1 and bridge-2 configurations, and 21 atoms for 2C-bond and 4C-atop ones, denoted as blue balls at Figure 10) and found them to accumulate up to 95.5% of total molecule charge (see Table 5). Bridge configurations are more polarized than more symmetric 2C-bond and 4C-atop, even though the latter ones have more atoms contacting with substrate (contacting atoms were chosen according to the fullerene's curvature in each case).

Since there are several structures being very close to each other, it makes sense to know how easy the fullerene can move from one to another. Potential barriers of

fullerene relocation were then calculated using NEB method (see Figure 13). Even though the lowest barriers correspond to transitions between two familiar configurations, and there is no potential barrier in 2C-bond – bridge-2 transition, other ones are still relatively low (<0.5 eV) so that fullerene can move freely along the surface.

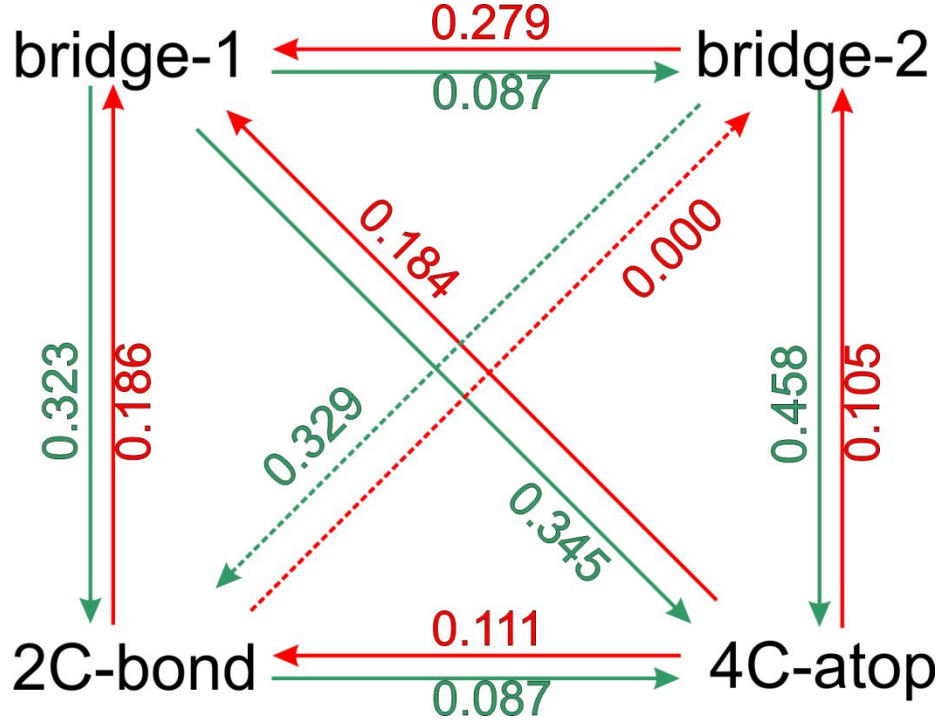


Figure 13. Potential barriers of C₆₀ relocation, eV

In order to estimate the movability of C₆₀ molecule, rate constant for the transition with the highest potential barrier (bridge-2 – 4C-atop) was calculated using transition state theory:

$$k = Ae^{-\frac{E_{\text{barrier}}}{kT}}, \quad (48)$$

where A was estimated as:

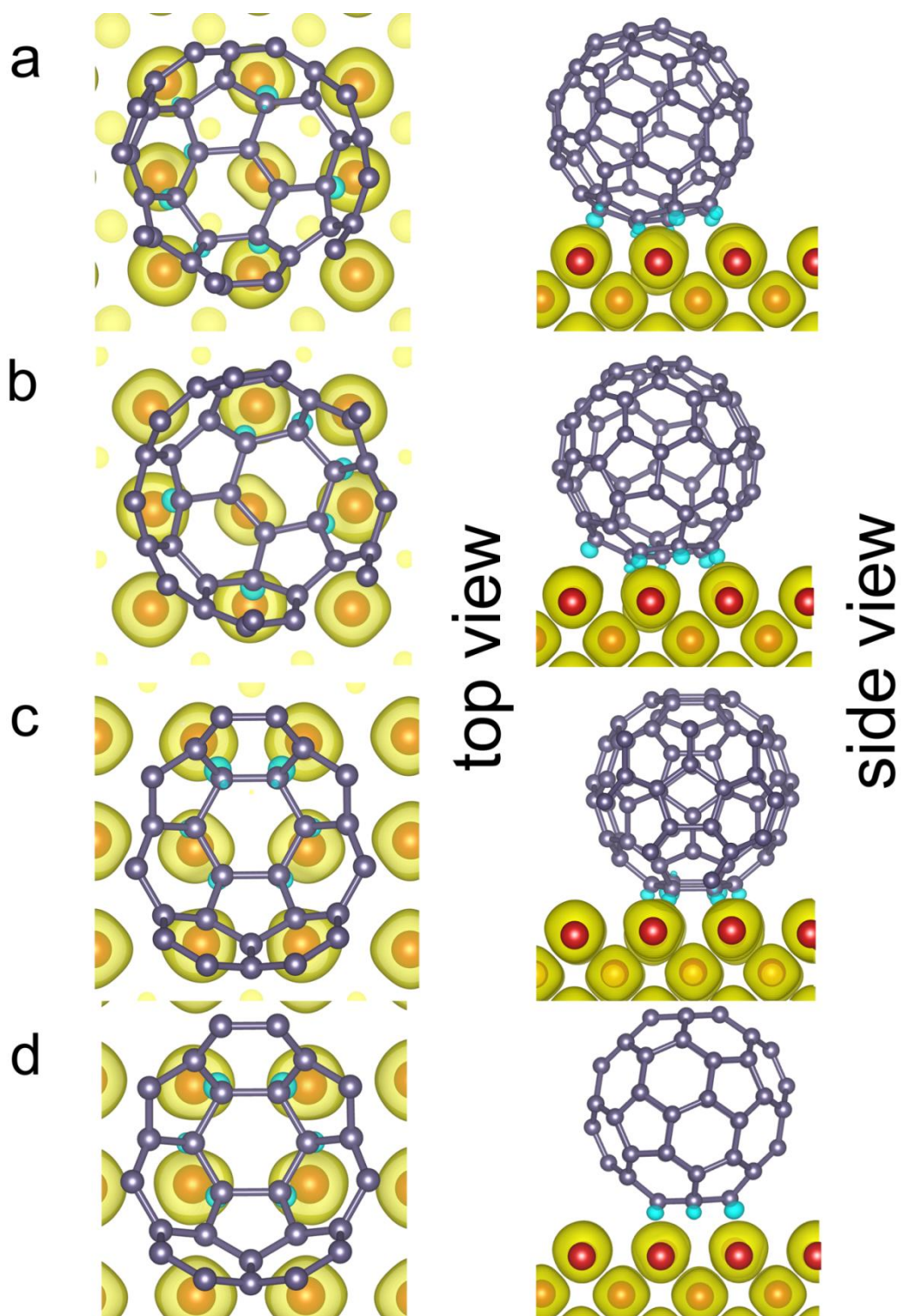


Figure 14. Spatial distribution of spin density in $C_{60}/Fe(001)$ composites for a) bridge-1; b) bridge-2; c) 2C-bond; d) 4C-atop configurations. Carbon and iron atoms are denoted as grey and red balls, respectively. Yellow (blue) areas correspond to spin-up (spin-down) density.

$$A = \frac{kT \prod_{i=1}^{3N-3} (1 - e^{-\frac{h\nu_i}{kT}})}{h \prod_{i=1}^{3N-4} (1 - e^{-\frac{h\nu_i^{\#}}{kT}})} \quad (49)$$

T is temperature, E_{barrier} is the potential barrier height calculated as the energy difference between transition state and initial composite, nominator product corresponds to the minimum energy points and denominator product corresponds to the transition state, ν_i is the frequency.

Zero-point energy was also taken into account when calculating potential barrier of fullerene's relocation by adding

$$E_i^{\#} = \sum_{i=1}^{3N-4} \frac{h\nu_i^{\#}}{2} \quad (50)$$

to transition state energy and

$$E_0 = \sum_{i=1}^{3N-3} \frac{h\nu_i}{2} \quad (51)$$

to the energy of initial structure. N is the number of atoms in system. Corrected by zero-point energy, potential barrier is equal to 0.468 eV.

According to our calculations, rate constant of C_{60} relocation from bridge-2 to 4C-atop position is equal to 105410 s^{-1} at 300K and 1521800 s^{-1} at 350K (A is equal to $7.7 \cdot 10^{12} \text{ s}^{-1}$). This means that, indeed, even for the highest barrier number of transitions per second is considerably large and should be even larger in other cases so that fullerene can freely move from one structure to another. It should be pointed out that it can adopt not only these four structures but there definitely should be some more configurations, though being very close both in energy and geometry. Indeed, it can be clearly seen from Figures 9 and 10 that a very small rotation is actually enough to transform, for example, 2C-bond structure to bridge-2. Another way to go from one configuration to another is to slide along the surface for considerably small distance (e.g. 2C-bond to 4C-atop transition). Thus,

the fullerene does not have to move for large distances, which is important since it's not isolated but there are neighboring molecules as well.

Keeping this in mind, we estimated relative probabilities of each state appearance according to the Gibbs distribution at the temperature range of 250 – 350 K:

$$P_i = \frac{e^{-\frac{E_i}{k_B T}}}{\sum_{i=1}^4 e^{-\frac{E_i}{k_B T}}}, \quad (52)$$

where E_i is the total energy of configuration i , T is the temperature, and k_B is the Boltzmann constant.

According to the values we obtained (see Table 6), P does not undergo any significant change from 250 to 350 K which is more than enough for nanoelectronic devices working in the narrow temperature range. It's also worth noting that all configurations are almost equally probable (~24-27%). This was taken into account when calculating average values of charge transfer, magnetic moment on the C_{60} molecule and its spin polarization at Fermi level:

$$X = P_i \cdot X_i, \quad (53)$$

where X is charge, magnetic moment or spin polarization, i indicates one of the four possible structures, P is the corresponding probability of its appearance. Both charge and magnetic moment were found to remain virtually the same with temperature increase. Stability of these two important characteristics of composite opens perspectives of using C_{60} deposited on Fe(001) as quantum dots, particularly, as possible qubits. Notwithstanding absolute values of spin polarization at Fermi level are relatively large in each case, its average value is only ~2.5% since ξ can be either positive or negative depending on the structure (see Table 5). It does depend on the temperature as well.

Table 6. Probability (P) of different configurations appearance, charge and magnetic moment versus temperature

P			
	Temperature, K		
	250	300	350
bridge-1	0.252	0.252	0.251
bridge-2	0.267	0.264	0.262
2C-bond	0.241	0.243	0.244
4C-atop	0.240	0.241	0.243
Averaged properties of C ₆₀ molecule			
	Temperature, K		
	250	300	350
Charge, e	1.982	1.980	1.980
Magnetic moment, μ_B	-0.119	-0.118	-0.118
Spin polarization at Fermi level, %	-2.4	-2.5	-2.5

4.3 Characterization of LSMO/C₆₀ nanocomposites

Different possible configurations of LSMO/C₆₀ nanocomposite were considered (see Figure 15). Each configuration is denoted as X(η^y), where X=O or Mn, and y stands for the number of carbon atoms surrounding X (see Figure 15). Five initial configurations with y varying from 2 to 6 were chosen for Mn-coordinated structures, and, similarly, for O-coordinated ones. Since there are two unequal η^2 configurations (with carbon bond between two hexagons or between hexagon and pentagon placed upon corresponding LSMO atoms), they were designated as η^2 and $\eta^{2'}$, respectively. Obviously, there is no way to construct an η^4 configuration with four carbon atoms being equally distant from coordinating

atom. Thus, it has been excluded from the scope of our investigation, and so the total number of initial structures became 10. According to our calculations, binding energies of all structures are considerably high and differ from each other in range of 0.3 eV (see Table 7). Such proximity witnesses the co-existence of many microstates that can easily transform from one to another (see Figure 15). The height of migration barrier is conditioned mainly by the difference in binding energies. Possibility of fullerene's migration along the surface was also recently reported for Au and Fe

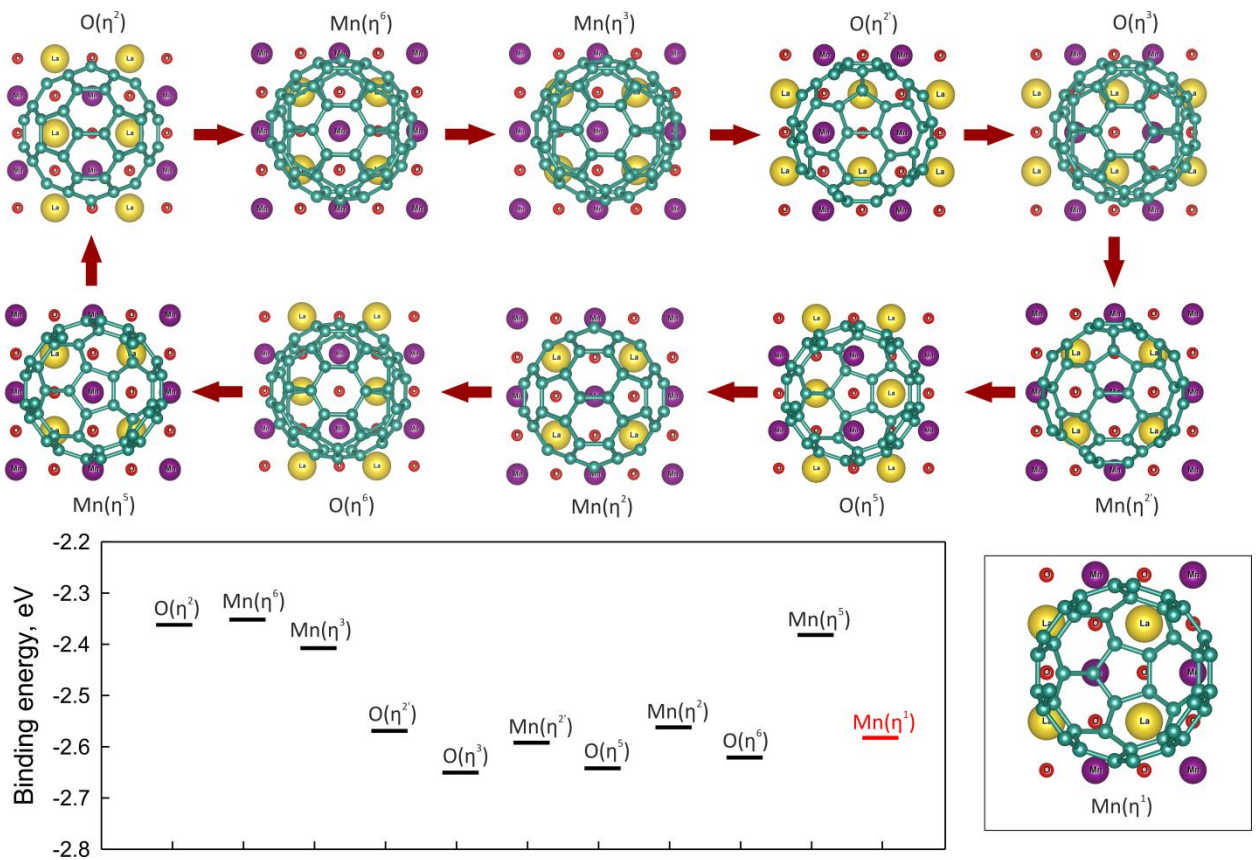


Figure 15. Possible geometries of LSMO/C₆₀ hybrid structures and binding energies corresponding to them. For the sake of better clarity, only the bottom part of the fullerene is presented, when needed. Inset shows additional structure with carbon atom placed upon Mn.

surfaces [113,114]. The probability of each state appearance was estimated according to the Gibbs distribution in the temperature range of 300-600 K. $O(\eta^3)$ and $O(\eta^5)$ were found to be the most probable to occur at 300 K. It can be noticed from Figure 15 that these two structures possess carbon atoms placed upon Mn atom, while structure with C-C bond upon the Mn atom are less favorable, and ones without contact with manganese atom are considerably higher in energy. This reveals the key role of transition metal atom in binding between LSMO and C_{60} molecule. At the same time, the presence of oxygen leads to repulsion with fullerene's π -conjugated system. Supply from $O(\eta^6)$ and $Mn(\eta^2)$ configurations

Table 7. Binding energy, fullerene's charge, magnetic moment and spin polarization at Fermi level in LSMO/ C_{60} nanocomposites

Type of structure	Binding energy, eV	C_{60} charge, e	C_{60} magnetic moment, μ_B	Spin polarization of C_{60} at Fermi level, %
$Mn(\eta^6)$	-2.3518	0.3261	0.0326	-4.7
$Mn(\eta^5)$	-2.3819	0.3361	0.0185	-13.7
$Mn(\eta^2)$	-2.5621	0.3389	0.0373	-6.6
$Mn(\eta^{2'})$	-2.5920	0.3661	0.0499	-20.1
$Mn(\eta^3)$	-2.4076	0.3340	0.0336	-5.9
$O(\eta^6)$	-2.6210	0.3603	0.0446	-13.0
$O(\eta^5)$	-2.6420	0.3698	0.0298	-21.9
$O(\eta^2)$	-2.3620	0.3165	0.0241	-3.8
$O(\eta^{2'})$	-2.5690	0.3544	0.0456	-11.0
$O(\eta^3)$	-2.6504	0.3703	0.0435	-18.3
$Mn(\eta^1)$	-2.5789	0.3576	0.0369	-24.5

becomes valuable as the temperature increases (18 and 10% at 600 K, respectively, see Table 8). Less pronounced are supplies from $O(\eta^{2'})$ and $Mn(\eta^2)$ (6% at 600 K). Probabilities of other configurations appearance are less than 5% even at 600 K.

Table 8. Probability (P) of each configuration appearance, fullerene's averaged charge, magnetic moment and spin polarization versus temperature.

P				
	Temperature, K			
	300	400	500	600
$Mn(\eta^6)$	less than 0.01	less than 0.01	less than 0.01	less than 0.01
$Mn(\eta^5)$	less than 0.01	less than 0.01	less than 0.01	less than 0.01
$Mn(\eta^2)$	0.01	0.03	0.04	0.06
$Mn(\eta^{2'})$	0.05	0.07	0.09	0.10
$Mn(\eta^3)$	less than 0.01	less than 0.01	less than 0.01	less than 0.01
$O(\eta^6)$	0.14	0.17	0.17	0.18
$O(\eta^5)$	0.32	0.30	0.29	0.27
$O(\eta^2)$	less than 0.01	less than 0.01	less than 0.01	less than 0.01
$O(\eta^{2'})$	0.02	0.03	0.05	0.06
$O(\eta^3)$	0.45	0.39	0.35	0.32
Averaged properties of C_{60} molecule				
	Temperature, K			
	300	400	500	600
Charge, e	0.3677	0.3666	0.3658	0.3648
Magnetic moment, μB	0.0394	0.0398	0.0401	0.0403
Spin polarization at Fermi level, %	-18.5 (-18.6)	-18.0 (-18.3)	-17.6 (-18.0)	-17.3 (-17.8)

The analysis of composites' electronic structure (see Table 7) shows that charge and magnetic moment on fullerene molecule is virtually the same for all configurations. Spin polarization value varies from 4 to 22% for different configuration.

However, it doesn't change its sign (see Table 7) that means that spin-polarized transport is possible even if one configuration moves to another. Averaged properties of fullerene molecule in LSMO/C₆₀ composite were calculated taking into account probabilities of microstates' appearance at different temperatures. All properties discussed here remain stable in the temperature range of 300 – 600 K (see Table 8). C₆₀ molecule gains the charge of approximately 0.36 e due to the interaction with LSMO slab, though it seems to be not spin-polarized according to the small value of magnetic moment ($\sim 0.04 \mu_B$). Spin density distribution analysis was then performed for two most favorable configurations (see Figure 16). Only carbon atoms being placed upon Mn possess negative spin polarization while adjacent atoms are positively spin-polarized resulting in relatively small total magnetic moment on the molecule. This confirms our suggestions about the key role of Mn atoms in binding between fullerene and LSMO substrate.

In order to prove this, we then performed the calculation of one more additional structure with pentagon carbon atom being placed directly upon Mn atom (Mn(η^1) configuration, see inset on Figure 15). Binding energy of this structure was found to lie in the range defined previously for structures with carbon upon manganese, though being lower than for O(η^3) and O(η^5) considered as the most favorable ones. This may be attributed to the fact that two manganese atoms are involved into the interaction in latter case (see Figure 2) instead of one in case of Mn(η^1).

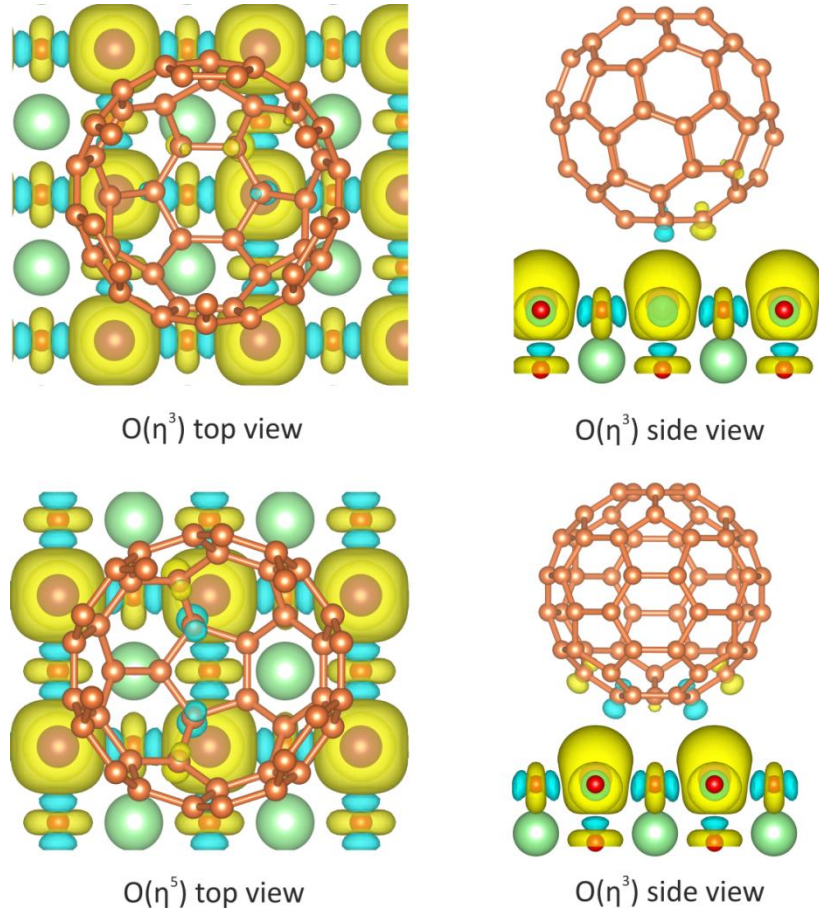


Figure 16. Spatial spin density distribution in LSMO/C₆₀ composites. Blue and yellow areas denote spin-up and spin-down density, respectively.

Properties of C₆₀ molecule for this configuration are summarized in Table 7 and red-colored since they were not included when calculating averaged properties for Table 8. We additionally calculated probability of its appearance and found it to vary from 3 to 7% for different temperatures. Including this configuration into averaging procedure does not affect neither charge nor magnetic moment on fullerene molecule but increases the degree of spin polarization at Fermi level, especially at high temperatures. These new values are then presented in parentheses in Table 8. Indeed, one can clearly see from Table 7 that new Mn(η^1) structure possesses the highest degree of spin polarization among all. Spin density

spatial distribution presented on Figure 17 is in perfect agreement with results previously obtained (see Figure 16).

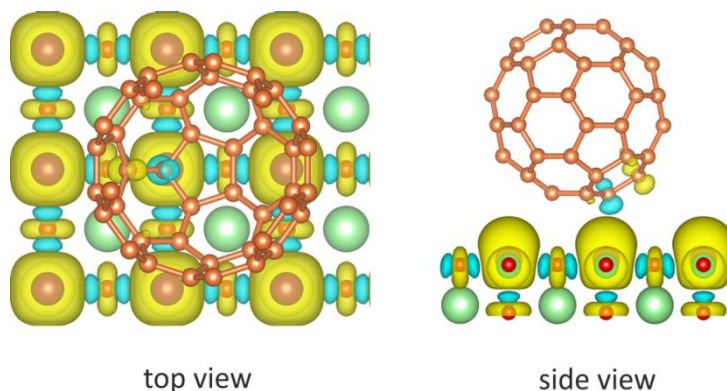


Figure 17. Spatial spin density distribution for $\text{Mn}(\eta^1)$ structure. Blue and yellow areas denote spin-up and spin-down density, respectively.

However, analysis of PDOS plotted for positively and negatively spin-polarized carbon atoms shows only the minor difference between them (see Figure 18a). Higher spin polarization at Fermi level for C atom adjacent to contacting is also quite puzzling and complicates the understanding of physics beyond this. This problem can be solved by integrating the DOS over the energies (which corresponds to how many states can be found below the given energy) and then taking the residual between spin-up and spin-down integrated DOS which gives the total spin polarization itself. Such analysis is presented on Figure 18b. Apparently, Mn atom affects contacting C atom making it negatively spin-polarized, and contacting C, in turn, affects adjacent carbon atom resulting into positive spin polarization of the latter. This can be seen from the perfect match between all the features in their spin polarization spectra. The abovementioned kind of magnetic ordering then spreads over the whole C_{60} molecule with decreasing intensity and can be seen from spatial spin density patterns when lowering isosurface level. In fact, complex magnetic exchange mechanism is involved. It appears to be very similar to superexchange interaction between 3d metal cations and nonmagnetic

anions but here the overlapping between manganese d_{z^2} orbitals and molecular orbitals of C_{60} molecule takes place (see Figure 18c). This gives us insight of how spin-polarized current flows through LSMO/ C_{60} interface though the total magnetic moment of fullerene molecule is considerably low.

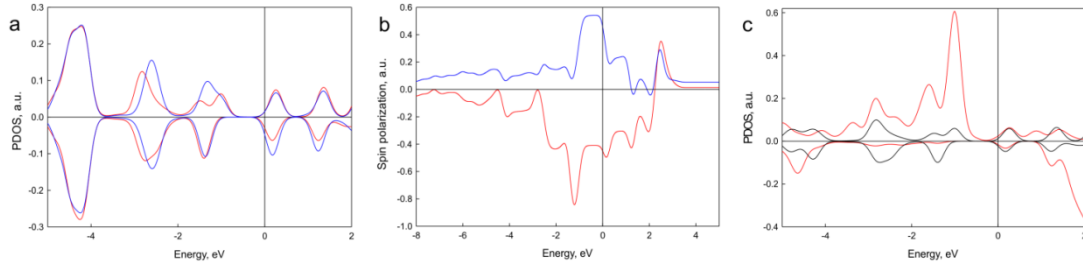
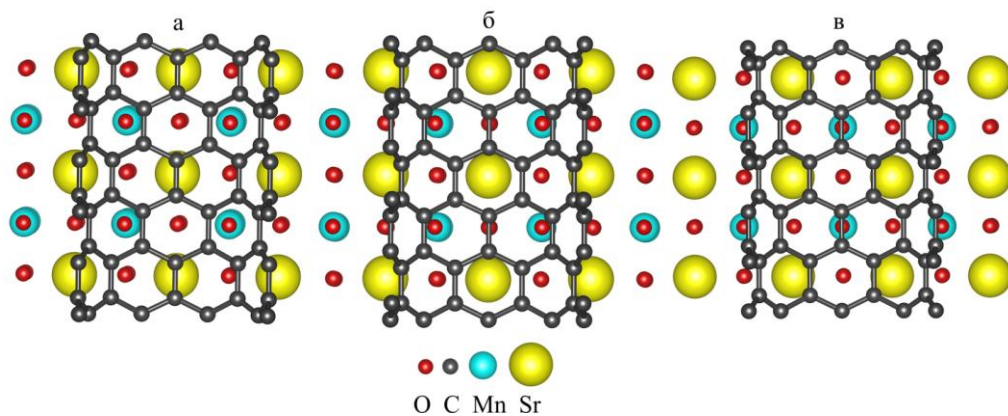


Figure 18. Partial density of states (a) and overall spin polarization (b) for C atom contacting with Mn (red line) and adjacent C atom (blue line); partial density of states (c) for Mn d_{z^2} (red line) and carbon p_z (black line) orbitals

4.4 The role of surface termination in CNT/LSMO composites

4.4.1 Interaction with Sr-O terminated surface

Three CNT(9,0)/LSMO(Sr-O) configurations (Figure 19) were considered. The first $Sr(\eta^2)$ configuration (Sr ion coordinated to C-C bond) is presented in Figure 19a. The second $Sr(\eta^3)$ configuration was originally characterized by Sr ion coordinated to carbon hexagon but slightly displaced during the optimization resulting in coordination to C_3 fragment of CNT(9,0) (Figure 19b). The third CNT(9,0) $O(\eta^{6-2})$ configuration with two oxygen ions coordinated to η^6 and η^2 positions, respectively, is presented in Figure 19c. It is necessary to note that the difference between lattice parameter of LSMO and CNT(9,0) along a direction is quite large and results in 9% contraction of the CNT(9,0).



a – $\text{Sr}(\eta^2)$, b – $\text{Sr}(\eta^3)$, B – $\text{O}(\eta^{6-2})$

Figure 19. Different configurations of CNT(9,0)/LSMO(Sr-O) nanocomposites.

For the sake of better representation, the upper part of tubes is cut.

Similarly to the interfaces of CNTs with ferromagnetic substrates of Co(0001) and Ni(111) [53,115], armchair (5,5) carbon nanotube being very close in diameter to CNT(9,0) (6,97 and 7,05 Å, respectively) was also considered. Only the $\text{Sr}(\eta^{6-2})$ configuration (Figure 20) was calculated for CNT(5,5)/LSMO(Sr-O) heterostructure since it is close to the most favourable for CNT(9,0)/LSMO(Sr-O) $\text{Sr}(\eta^3)$ configuration. The CNT (5,5) slab is stretched by 5% because of mismatch with the structural parameters of LSMO. The binding energies and shortest bond lengths between CNT and LSMO fragments for CNT-based heterostructures are presented in Table 9.

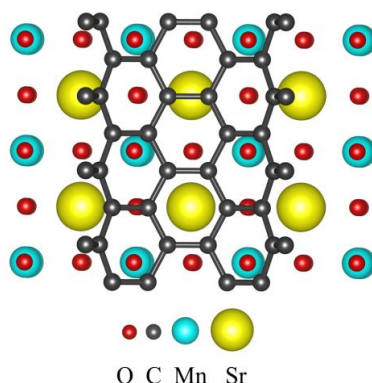


Figure 20. Structure of CNT(5,5)/LSMO(Sr-O) nanocomposite. For the sake of better representation, the upper part of the tube is cut.

Values of binding energies and bond distances witness the presence of weak van der Waals interactions between CNTs and LSMO slab (Table 9).

Table 9. Binding energies and bond lengths of CNT(9,0)/LSMO(Sr-O) and CNT(5,5)/LSMO(Sr-O) heterostructures

Composite	CNT(9,0)/LSMO			CNT(5,5)/LSMO
	Sr(η^3)	O(η^{6-2})	Sr(η^2)	
Binding energy, eV	-0.5663	-0.3468	1.0213	-2.0710
Bond distance, Å	2.830	3.023	2.898	3.123

Configuration Sr(η^3) is the most energetically favorable among three CNT(9,0)/LSMO(Sr-O) composites with -0.5663 eV binding energy per supercell (which corresponds to -0.016 eV/carbon atom). Strontium atom is displaced from the centre of carbon hexagon to attain the η^3 site changing Sr(η^6) configuration to Sr(η^3), so the bond length becomes shorter (see Figure 19b). However, Sr(η^2) configuration with comparable bond distance is not stable because of positive binding energy (1.0213 eV or 0.028 eV per carbon atom).

The Sr(η^{6-2}) configuration of CNT(5,5)/LSMO(Sr-O) heterostructure demonstrates lower binding energy (-2.0710 eV per unit cell or -0.035 eV per carbon atom). No displacement was observed for this configuration. It is necessary to note that CNT(9,0) and CNT(5,5) have almost the same diameter and they do not create covalent bonds with LSMO support. So, the visible difference in the binding energies of the nanotubes can be caused by different types and values of structural stress caused by crystal lattice mismatch.

The analysis of composites' electronic structure (Figure 21) shows that it remains almost the same as for bare LSMO in both cases. Only a slight peak

displacement can be observed. Although composites are almost totally spin polarized, it can be seen that this is due to LSMO slab while nanotubes' spin-up and spin-down partial densities of states are of an equal intensity (spin polarization values are $\sim 1.7\%$ and $\sim 0.3\%$ for CNT(5,5) and CNT(9,0), respectively, the absence of visible spin polarization is also confirmed by the spatial spin density distribution).

To study the influence of the associated strain, the free-standing relaxed and stretched (the same stress as for CNTs on LSMO) CNT(9,0) and CNT(5,5) were chosen for the calculations. It should be noticed that stretching and contraction of bare nanotubes leads to the rearrangement of electron density, then unoccupied bands are filled and the Fermi level changes (Figure 22). Similar effect is observed when it's interacting with LSMO. The strain leads to appearance of a narrow band gap (0.2 eV) and significant shift of the Fermi level in the DOS of CNT(5,5) (Figure 22a). Interaction of CNT(5,5) with LSMO fragment leads to the visible redistribution of peak intensities of the DOS with low spin polarization at Fermi level (1.7%). The same effects are detected for CNT(9,0) as well.

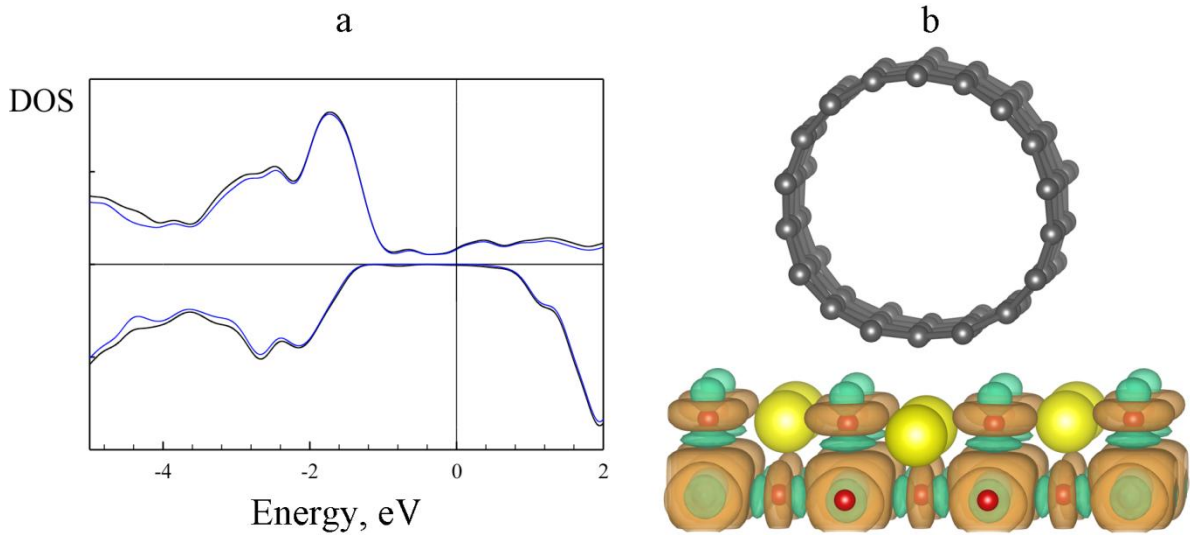


Figure 21. a) Density of states of CNT(9,0)/LSMO(Sr-O) heterostructure. Black and blue lines correspond to the total and partial LSMO DOS, respectively. b) Spatial distribution of spin density in CNT(5,5)/LSMO(Sr-O) heterostructure.

Grey, yellow and red balls correspond to carbon, strontium and oxygen atoms; green and brown areas represent spin-up and spin-down density, respectively.

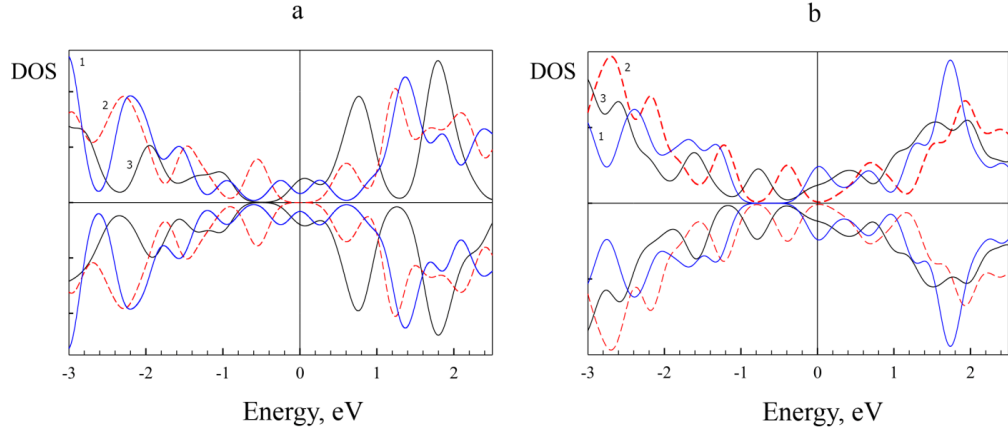


Figure 22. Densities of states for (a) CNT(5,5) and (b) CNT(9,0). Blue, red and black lines correspond to relaxed CNTs structures, strained CNTs structures with LSMO translation vector adopted, and partial densities of states of nanotubes in CNT/LSMO(Sr-O) composite.

The contraction leads to the visible shift of Fermi level, and interaction with LSMO causes further shift and smearing of peaks. The spin polarization of the CNT(9,0) is even smaller than for CNT(5,5) and is equal to 0.3%. The Bader charge analysis [110–112] shows that total tube charges are equal to 0.4 and 0.8 electron charges for CNT(9,0)/LSMO and CNT(5,5)/LSMO, respectively.

Thus, even though the substrate changes the electronic structure of the nanotubes significantly, there is no difference between spin-up and spin-down density, in contrast to ferromagnetic Co(0001) and Ni(111) surfaces [53,115]. The electronic structure of LSMO is also virtually the same as for pristine slab confirming the presence of a weak van-der-Waals interaction between Sr-O terminated LSMO and carbon nanotubes. However, a different termination may lead to the new interesting effects and change the composite properties. Hence, we then considered interaction of CNT(5,5) with Mn-O terminated LSMO surface.

4.4.2 Interaction with Mn-O terminated surface

Keeping in mind the fact of a major contraction of CNT(9,0) when forming composites with $\text{La}_{0.7}\text{Sr}_{0.3}\text{MnO}_3$, we then decided to pay more attention for interaction between CNT(5,5) and Mn-O terminated LSMO. As previously, $6 \times 2 \times 1$ supercell ($a = 23.32 \text{ \AA}$, $b = 7.77 \text{ \AA}$, $c = 30.00 \text{ \AA}$) of LSMO slab was used with $1 \times 2 \times 1$ k -points along a , b and c direction.

We have considered three following configurations of CNT(5,5)/LSMO(Mn-O) composite (Figure 23): $\text{Mn}(\eta^{6-2})$ with Mn atoms coordinated to carbon hexagon and C-C bond (see Figure 23a); $\text{O}(\eta^4)$ with oxygen atom being slightly displaced from the center of hexagon (see Figure 23b); and $\text{O}(\eta^{6-2})$ configuration with oxygen atoms coordinated to η^6 and η^2 positions (see Figure 23c).

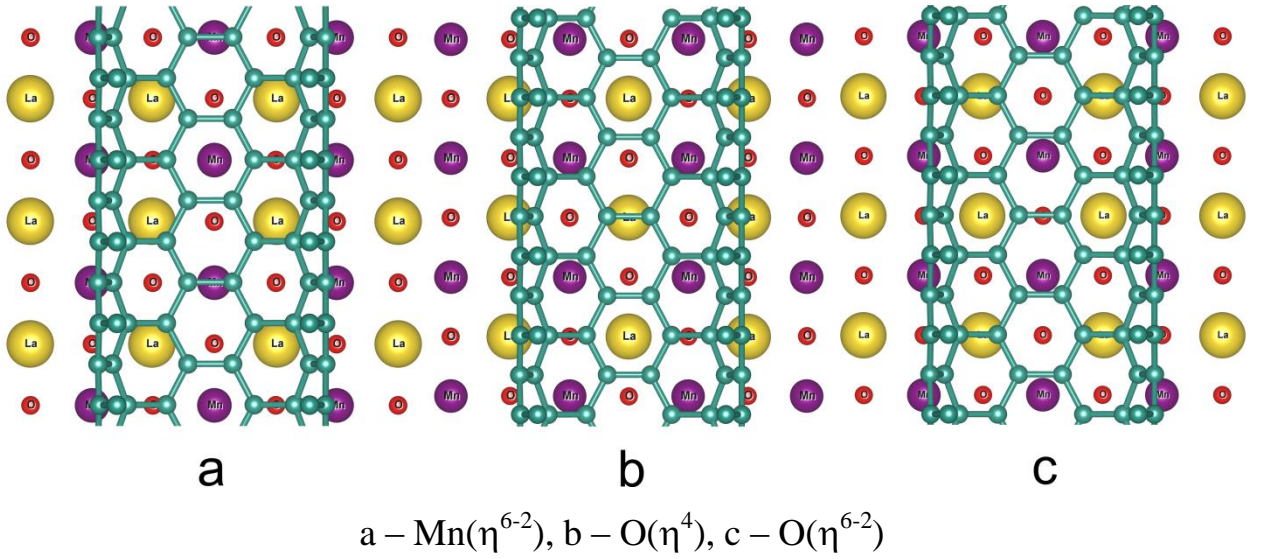


Figure 23. Configurations of CNT(5,5)/LSMO(Mn-O) nanocomposite. For the sake of better representation, the upper part of the tube is cut.

According to our calculations, $\text{O}(\eta^4)$ is the most favorable among all (see Table 2) even though it demonstrates larger bond distance in comparison with $\text{Mn}(\eta^{6-2})$ and $\text{O}(\eta^{6-2})$ ones. This may be explained in terms of stronger interaction between nanotube carbon conjugated system and manganese ions (see Figure 4 and Figure 6). Indeed, we can clearly see that while there is only one Mn atom

overlapping with each carbon hexagon in $\text{Mn}(\eta^{6-2})$ and $\text{O}(\eta^{6-2})$, each hexagon of $\text{O}(\eta^4)$ contacts with two manganese atoms. The patterns of spin density distribution (Figure 6) support this suggestion: we can see negative spin polarization of carbon atoms contacting with manganese and positive spin polarizations of atoms next to them, which is very similar to what we have observed for buckminsterfullerene deposited on the same surface [116].

Table 10. Properties of CNT(5,5)/LSMO(Mn-O) nanocomposite

Composite	CNT(5,5)/LSMO		
	$\text{Mn}(\eta^{6-2})$	$\text{O}(\eta^4)$	$\text{O}(\eta^{6-2})$
Binding energy, eV	-1,25	-1,41	-1,23
Bond distance, Å	2,53	2,70	2,65
Charge of the tube, e	0,25	0,28	0,24
Magnetic moment of the tube, μ_B	0,15	0,12	0,13
Spin polarization of the tube at the Fermi level, %	-12,8	-44,2	-12,6

Configuration $\text{O}(\eta^4)$ possesses slightly larger charge being transferred to the tube and much larger spin polarization at the Fermi level, in contrast to both Sr-O terminated surface and other two configurations (see Table 10). The magnetic moment on the tube is, however, slightly smaller than others. This is obviously caused by the effect we've mentioned above: there are both positively and negatively spin-polarized carbon atoms, and the stronger is the interaction between manganese and carbon, the more prominent becomes the complex magnetic ordering previously found for carbon structures on LSMO(Mn-O) surface. Since

the $O(\eta^4)$ is the most symmetric with respect to the Mn, positive and negative spin polarization partially compensate each other. However, one could have noticed that binding energy for the CNT(5,5) on LSMO(Mn-O) surface are by $\sim 0.7-0.8$ eV smaller than that for CNT(5,5) on LSMO(Sr-O) surface even though the interaction between composite compartments is stronger in former case. This is mainly caused by the major deformation of the tubes when forming these composites (see Figure 24). The energy of nanotube's deformation was estimated to vary from 0.4 to 0.5 depending on the configuration, and, thus, was supposed to be responsible for the difference in binding energy.

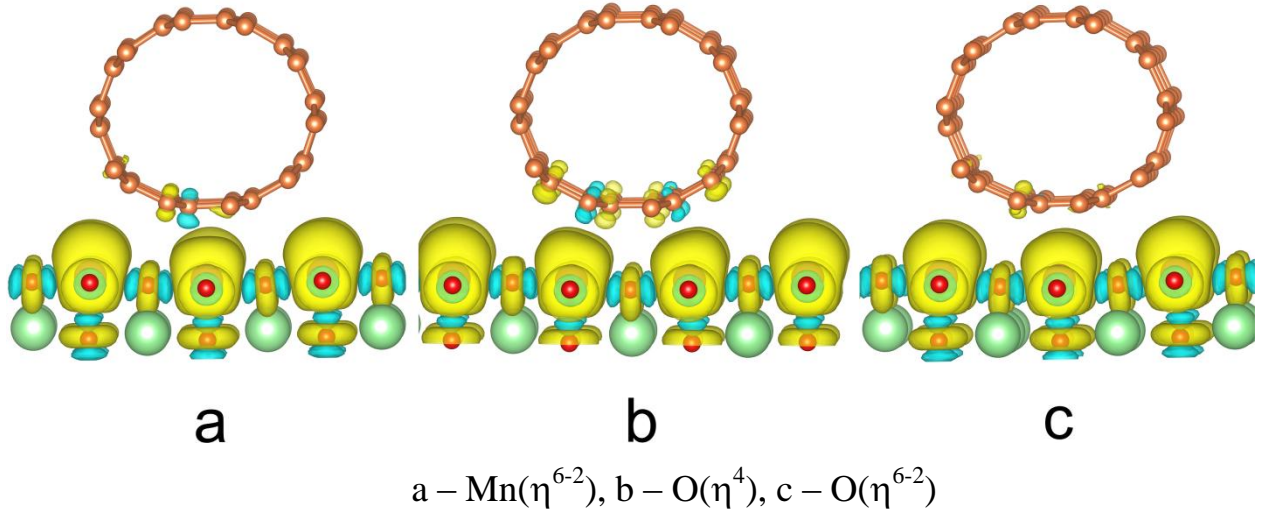


Figure 24. Spatial spin density distribution in CNT(5,5)/LSMO(Mn-O) nanocomposites. Yellow and blue areas correspond to spin-up and spin-down density, respectively.

SUMMARY

The interfaces of armchair and zigzag carbon and boron nitride nanotubes with ferromagnetic Co(0001) and Ni(111) surfaces was investigated by first-principles calculations. The electronic structure analysis reveals the presence of contact-induced spin polarization in all composites. It was found that NT(n,0)/Co composites are approximately twice as low in energy as NT(n,0)/Ni ones and spin polarization in these systems is also much stronger. Lower energy of CNT(9,0)/TM in comparison with CNT(10,0)/TM can be attributed to the difference in their conducting properties. Conducting nature of CNT(9,0) also causes a weaker spin polarization in comparison with other tubes. In addition, BNNTs demonstrate a local contact-induced conductivity while the fragments distant from interface remain to be insulating. Value of spin polarization differs significantly from one possible configuration of composite to another for armchair nanotubes. Unfortunately, for all considered systems there is almost no difference in energy among the variants of nanotube and metal substrate mutual arrangement. This makes their utilization in spintronics unreasonable, in contrast with previously studied zigzag nanotubes [8]. However, contact-induced local conductivity in boron nitride nanotubes still can be used somewhere in nanoelectronic devices. Particularly, their high thermal conductivity along with abovementioned unique electronic properties allows using them in thermoelectric coolers based on the Peltier effect.

Density functional study of atomic and electronic structure of C₆₀/Fe(100) composite shows the coexistence of a number of possible structures with strong chemical bonding between composite compartments. Fullerene and slab deformation plays an important role in the formation of composites. Low potential barriers of fullerene's relocation witness the

possibility of transitions between stable structures which are almost equally probable according to the Gibbs distribution. Average charge transfer and magnetic moment on C_{60} molecule remain virtually the same within the range of 250 – 350 K, opening possibility of using such composites for quantum computing or other applications. Many possible structures were also found to co-exist for LSMO/ C_{60} nanocomposites in wide range of temperatures. Only spin polarization at Fermi level was found to depend strongly on the configuration while both C_{60} charge and magnetic moment remain virtually the same. However, spin-polarized transport is still possible even for less favorable configurations. Manganese atoms play a key role in binding between fullerene and LSMO which is confirmed by the values of binding energies and spatial spin density distribution patterns. The mechanism of spin-polarized charge transport was discussed. According to our analysis of magnetic moment values and spin density spatial distribution, it's evident that this is due to the special kind of magnetic ordering in C_{60} molecule rising from the interaction with manganese atoms and complex magnetic exchange interaction.

The interaction with LSMO(Sr-O) slab changes the electronic structure of the tubes noticeably. However, this change is mainly due to the deformation of the tubes, not the interaction with the substrate. The electronic structure of LSMO remains unchanged, and only a weak van-der-Waals interaction is responsible for the composite formation. In contrast to the Sr-O terminated surface, there is a visible interaction between CNT(5,5) and Mn-O terminated LSMO. Overlapping between carbon and manganese atoms plays a key role in composite formation, in agreement with results obtained for C_{60} [116]. Regardless the major deformation of nanotubes when interacting with LSMO, the composite formation is energetically favorable in all cases.

REFERENCES

- [1] P. Hohenberg, W. Kohn, Inhomogeneous Electron Gas, *Phys. Rev.* 136 (1964) B864–B871. doi:10.1103/PhysRev.136.B864.
- [2] N.D. Mermin, Thermal Properties of the Inhomogeneous Electron Gas, *Phys. Rev.* 137 (1965) A1441–A1443. doi:10.1103/PhysRev.137.A1441.
- [3] W. Kohn, L.J. Sham, Self-Consistent Equations Including Exchange and Correlation Effects, *Phys. Rev.* 140 (1965) A1133–A1138. doi:10.1103/PhysRev.140.A1133.
- [4] L.J. Sham, W. Kohn, One-Particle Properties of an Inhomogeneous Interacting Electron Gas, *Phys. Rev.* 145 (1966) 561–567. doi:10.1103/PhysRev.145.561.
- [5] J.P. Perdew, A. Zunger, Self-interaction correction to density-functional approximations for many-electron systems, *Phys. Rev. B.* 23 (1981) 5048–5079. doi:10.1103/PhysRevB.23.5048.
- [6] J.P. Perdew, K. Burke, M. Ernzerhof, Generalized Gradient Approximation Made Simple, *Phys. Rev. Lett.* 77 (1996) 3865–3868. doi:10.1103/PhysRevLett.77.3865.
- [7] Y. Wang, J.P. Perdew, Spin scaling of the electron-gas correlation energy in the high-density limit, *Phys. Rev. B.* 43 (1991) 8911–8916. doi:10.1103/PhysRevB.43.8911.
- [8] S. Grimme, J. Antony, S. Ehrlich, H. Krieg, A consistent and accurate ab initio parametrization of density functional dispersion correction (DFT-D) for the 94 elements H-Pu, *J. Chem. Phys.* 132 (2010) 154104. doi:10.1063/1.3382344.
- [9] O. Gritsenko, E.J. Baerends, A simple natural orbital mechanism of “pure” van der Waals interaction in the lowest excited triplet

- state of the hydrogen molecule., J. Chem. Phys. 124 (2006) 54115.
doi:10.1063/1.2165183.
- [10] A.D. Becke, E.R. Johnson, A density-functional model of the dispersion interaction., J. Chem. Phys. 123 (2005) 154101. doi:10.1063/1.2065267.
- [11] J.G. Ángyán, I.C. Gerber, A. Savin, J. Toulouse, van der Waals forces in density functional theory: Perturbational long-range electron-interaction corrections, Phys. Rev. A. 72 (2005) 12510.
doi:10.1103/PhysRevA.72.012510.
- [12] M.A. Basanta, Y.J. Dappe, J. Ortega, F. Flores, Van der Waals forces in the local-orbital Density Functional Theory, Europhys. Lett. 70 (2005) 355–361.
doi:10.1209/epl/i2004-10495-7.
- [13] O.A. von Lilienfeld, I. Tavernelli, U. Rothlisberger, D. Sebastiani, Optimization of Effective Atom Centered Potentials for London Dispersion Forces in Density Functional Theory, Phys. Rev. Lett. 93 (2004) 153004.
doi:10.1103/PhysRevLett.93.153004.
- [14] S. Grimme, Accurate description of van der Waals complexes by density functional theory including empirical corrections, J. Comput. Chem. 25 (2004) 1463–1473. doi:10.1002/jcc.20078.
- [15] U. Zimmerli, M. Parrinello, P. Koumoutsakos, Dispersion corrections to density functionals for water aromatic interactions., J. Chem. Phys. 120 (2004) 2693–2699. doi:10.1063/1.1637034.
- [16] M. Elstner, P. Hobza, T. Frauenheim, S. Suhai, E. Kaxiras, Hydrogen bonding and stacking interactions of nucleic acid base pairs: A density-functional-theory based treatment, J. Chem. Phys. 114 (2001) 5149.
doi:10.1063/1.1329889.
- [17] S. Grimme, Semiempirical GGA-type density functional constructed with a long-range dispersion correction, J. Comput. Chem. 27 (2006) 1787–1799.
doi:10.1002/jcc.20495.

- [18] B. Himmetoglu, A. Floris, S. De Gironcoli, M. Cococcioni, Hubbard-corrected DFT energy functionals: The LDA+U description of correlated systems, *Int. J. Quantum Chem.* 114 (2014) 14–49. doi:10.1002/qua.24521.
- [19] S.L. Dudarev, G.A. Botton, S.Y. Savrasov, C.J. Humphreys, A.P. Sutton, Electron-energy-loss spectra and the structural stability of nickel oxide: An LSDA+U study, *Phys. Rev. B.* 57 (1998) 1505–1509. doi:10.1103/PhysRevB.57.1505.
- [20] J.C. Phillips, Energy-Band Interpolation Scheme Based on a Pseudopotential, *Phys. Rev.* 112 (1958) 685–695. doi:10.1103/PhysRev.112.685.
- [21] M.T. Yin, M.L. Cohen, Theory of *ab initio* pseudopotential calculations, *Phys. Rev. B.* 25 (1982) 7403–7412. doi:10.1103/PhysRevB.25.7403.
- [22] M.C. Payne, M.P. Teter, D.C. Allan, T.A. Arias, J.D. Joannopoulos, Iterative minimization techniques for *ab initio* total-energy calculations: molecular dynamics and conjugate gradients, *Rev. Mod. Phys.* 64 (1992) 1045–1097. doi:10.1103/RevModPhys.64.1045.
- [23] N. Troullier, J.L. Martins, Efficient pseudopotentials for plane-wave calculations, *Phys. Rev. B.* 43 (1991) 1993–2006. doi:10.1103/PhysRevB.43.1993.
- [24] R. Car, M. Parrinello, Unified Approach for Molecular Dynamics and Density-Functional Theory, *Phys. Rev. Lett.* 55 (1985) 2471–2474. doi:10.1103/PhysRevLett.55.2471.
- [25] D.R. Hamann, M. Schlüter, C. Chiang, Norm-Conserving Pseudopotentials, *Phys. Rev. Lett.* 43 (1979) 1494–1497. doi:10.1103/PhysRevLett.43.1494.
- [26] G.B. Bachelet, D.R. Hamann, M. Schlüter, Pseudopotentials that work: From H to Pu, *Phys. Rev. B.* 26 (1982) 4199–4228. doi:10.1103/PhysRevB.26.4199.
- [27] S. Goedecker, K. Maschke, Transferability of pseudopotentials, *Phys. Rev. A.* 45 (1992) 88–93. doi:10.1103/PhysRevA.45.88.

- [28] D. Vanderbilt, Soft self-consistent pseudopotentials in a generalized eigenvalue formalism, *Phys. Rev. B.* 41 (1990) 7892–7895.
doi:10.1103/PhysRevB.41.7892.
- [29] P.E. Blöchl, Projector augmented-wave method, *Phys. Rev. B.* 50 (1994) 17953–17979. doi:10.1103/PhysRevB.50.17953.
- [30] G. Kresse, D. Joubert, From ultrasoft pseudopotentials to the projector augmented-wave method, *Phys. Rev. B.* 59 (1999) 1758–1775.
doi:10.1103/PhysRevB.59.1758.
- [31] D.F. Shanno, R. Fletcher, M.J.D. Powell, C.G. Broyden, J.G.P. Barnes, F.J. Zeleznik, M.J. Box, C.G. Broyden, D. Goldfarb, D.F. Shanno, P.C. Kettler, Conditioning of quasi-Newton methods for function minimization, *Math. Comput.* 24 (1970) 647–656. doi:10.1090/S0025-5718-1970-0274029-X.
- [32] D. Goldfarb, C.G. Broyden, W.C. Davidon, R. Fletcher, M.J.D. Powell, D. Goldfarb, J. Greenstadt, A family of variable-metric methods derived by variational means, *Math. Comput.* 24 (1970) 23–26. doi:10.1090/S0025-5718-1970-0258249-6.
- [33] R. Fletcher, A new approach to variable metric algorithms, *Comput. J.* 13 (1970) 317–322. doi:10.1093/comjnl/13.3.317.
- [34] C.G. BROYDEN, The Convergence of a Class of Double-rank Minimization Algorithms 1. General Considerations, *IMA J. Appl. Math.* 6 (1970) 76–90.
doi:10.1093/imamat/6.1.76.
- [35] L.R. Pratt, A statistical method for identifying transition states in high dimensional problems, *J. Chem. Phys.* 85 (1986) 5045–5048.
doi:10.1063/1.451695.
- [36] R. Elber, M. Karplus, A method for determining reaction paths in large molecules: Application to myoglobin, *Chem. Phys. Lett.* 139 (1987) 375–380. doi:10.1016/0009-2614(87)80576-6.
- [37] L. Xie, H. Liu, W. Yang, Adapting the nudged elastic band method for

- determining minimum-energy paths of chemical reactions in enzymes., J. Chem. Phys. 120 (2004) 8039–8052. doi:10.1063/1.1691404.
- [38] G. Henkelman, H. Jónsson, A dimer method for finding saddle points on high dimensional potential surfaces using only first derivatives, J. Chem. Phys. 111 (1999) 7010–7022.
- [39] L.J. Munro, D.J. Wales, Defect migration in crystalline silicon, Phys. Rev. B. 59 (1999) 3969–3980. doi:10.1103/PhysRevB.59.3969.
- [40] G. Henkelman, H. Jónsson, Improved tangent estimate in the nudged elastic band method for finding minimum energy paths and saddle points, J. Chem. Phys. 113 (2000) 9978–9985. doi:10.1063/1.1323224.
- [41] G. Henkelman, B.P. Uberuaga, H. Jónsson, A climbing image nudged elastic band method for finding saddle points and minimum energy paths, J. Chem. Phys. 113 (2000) 9901–9904. doi:10.1063/1.1329672.
- [42] V.M. Karpan, P.A. Khomyakov, A.A. Starikov, G. Giovannetti, M. Zwierzycki, M. Talanana, G. Brocks, J. van den Brink, P.J. Kelly, Theoretical prediction of perfect spin filtering at interfaces between close-packed surfaces of Ni or Co and graphite or graphene, Phys. Rev. B. 78 (2008) 195419. doi:10.1103/PhysRevB.78.195419.
- [43] P. V. Avramov, A.A. Kuzubov, S. Sakai, M. Ohtomo, S. Entani, Y. Matsumoto, H. Naramoto, N.S. Eleseeva, Contact-induced spin polarization in graphene/h-BN/Ni nanocomposites, J. Appl. Phys. 112 (2012) 114303. doi:10.1063/1.4767134.
- [44] M. Fuentes-Cabrera, M.I. Baskes, A. V. Melechko, M.L. Simpson, Bridge structure for the graphene/Ni(111) system: A first principles study, Phys. Rev. B. 77 (2008) 35405. doi:10.1103/PhysRevB.77.035405.
- [45] M. Weser, Y. Rehder, K. Horn, M. Sicot, M. Fonin, A.B. Preobrajenski, E.N. Voloshina, E. Goering, Y.S. Dedkov, Induced magnetism of carbon atoms at the graphene/Ni(111) interface, Appl. Phys. Lett. 96 (2010) 12504.

doi:10.1063/1.3280047.

- [46] N. Joshi, P. Ghosh, Substrate-induced changes in the magnetic and electronic properties of hexagonal boron nitride, *Phys. Rev. B.* 87 (2013) 235440.
doi:10.1103/PhysRevB.87.235440.
- [47] E. Rokuta, Y. Hasegawa, K. Suzuki, Y. Gamou, C. Oshima, A. Nagashima, Phonon Dispersion of an Epitaxial Monolayer Film of Hexagonal Boron Nitride on Ni(111), *Phys. Rev. Lett.* 79 (1997) 4609–4612.
doi:10.1103/PhysRevLett.79.4609.
- [48] Y.G. Zhou, X.T. Zu, F. Gao, Substrate-induced magnetism in BN layer: A first-principles study, 2011. doi:10.1016/j.ssc.2011.04.001.
- [49] M. Hasegawa, K. Nishidate, Transfer doping of a metallic carbon nanotube and graphene on metal surfaces, *Phys. Rev. B.* 83 (2011) 155435.
doi:10.1103/PhysRevB.83.155435.
- [50] Y. Takagi, S. Okada, Electronic structure of single-walled carbon nanotube on metal surfaces by first principles calculations, *Phys. Status Solidi.* 8 (2011) 564–566. doi:10.1002/pssc.201000470.
- [51] S. Okada, A. Oshiyama, Electronic Structure of Semiconducting Nanotubes Adsorbed on Metal Surfaces, *Phys. Rev. Lett.* 95 (2005) 206804.
doi:10.1103/PhysRevLett.95.206804.
- [52] S.L.T. Jones, G. Greene-Diniz, M. Haverty, S. Shankar, J.C. Greer, Effect of structure on electronic properties of the iron-carbon nanotube interface, *Chem. Phys. Lett.* 615 (2014) 11–15. doi:10.1016/j.cplett.2014.09.056.
- [53] A.A. Kuzubov, E.A. Kovaleva, P. Avramov, A. V. Kuklin, N.S. Mikhaleva, F.N. Tomilin, S. Sakai, S. Entani, Y. Matsumoto, H. Naramoto, Contact-induced spin polarization in BNNT(CNT)/TM (TM=Co, Ni) nanocomposites, *J. Appl. Phys.* 116 (2014).
- [54] M. David, T. Kishi, M. Kisaku, W.A. Diño, H. Nakanishi, H. Kasai, First principles investigation on Fe-filled single-walled carbon nanotubes on Ni

- (111) and Cu (111), *J. Magn. Magn. Mater.* 310 (2007) e748–e750.
doi:10.1016/j.jmmm.2006.10.755.
- [55] G.P. Soares, Structural and Electronic Properties of Impurities on Boron Nitride Nanotube, *J. Mod. Phys.* 2 (2011) 857–863.
doi:10.4236/jmp.2011.28102.
- [56] A. Nagashima, N. Tejima, Y. Gamou, T. Kawai, C. Oshima, Electronic dispersion relations of monolayer hexagonal boron nitride formed on the Ni(111) surface, *Phys. Rev. B.* 51 (1995) 4606–4613.
doi:10.1103/PhysRevB.51.4606.
- [57] W.J.M. Naber, S. Faez, W.G. van der Wiel, W.G. Van Der Wiel, Organic spintronics, *J. Phys. D. Appl. Phys.* 40 (2007) R205–R228.
doi:10.1088/0022-3727/40/12/R01.
- [58] V. Dediu, M. Murgia, F.C. Maticcotta, C. Taliani, S. Barbanera, Room temperature spin polarized injection in organic semiconductor, *Solid State Commun.* 122 (2002) 181–184. doi:10.1016/S0038-1098(02)00090-X.
- [59] V.A. Dediu, L.E. Hueso, I. Bergenti, C. Taliani, Spin routes in organic semiconductors., *Nat. Mater.* 8 (2009) 707–16. doi:10.1038/nmat2510.
- [60] T.D. Nguyen, G. Hukic-Markosian, F. Wang, L. Wojcik, X.-G. Li, E. Ehrenfreund, Z.V. Vardeny, Isotope effect in spin response of pi-conjugated polymer films and devices., *Nat. Mater.* 9 (2010) 345–352.
doi:10.1038/nmat2633.
- [61] Z.H. Xiong, D. Wu, Z.V. Vardeny, J. Shi, Giant magnetoresistance in organic spin-valves, *Nature.* 427 (2004) 821–824.
doi:10.1038/nature02277.1.
- [62] V. Dediu, L.E. Hueso, I. Bergenti, A. Riminucci, F. Borgatti, P. Graziosi, C. Newby, F. Casoli, M.P. De Jong, C. Taliani, Y. Zhan, Room-temperature spintronic effects in Alq₃ -based hybrid devices, *Phys. Rev. B - Condens. Matter Mater. Phys.* 78 (2008). doi:10.1103/PhysRevB.78.115203.

- [63] C. Barraud, P. Seneor, R. Mattana, S. Fusil, K. Bouzehouane, C. Deranlot, P. Graziosi, L. Hueso, I. Bergenti, V. Dediu, F. Petroff, A. Fert, Unravelling the role of the interface for spin injection into organic semiconductors, *Nat. Phys.* 6 (2010) 615–620. doi:10.1038/nphys1688.
- [64] J.J.H.M. Schoonus, P.G.E. Lumens, W. Wagemans, J.T. Kohlhepp, P.A. Bobbert, H.J.M. Swagten, B. Koopmans, Magnetoresistance in hybrid organic spin valves at the onset of multiple-step tunneling, *Phys. Rev. Lett.* 103 (2009). doi:10.1103/PhysRevLett.103.146601.
- [65] M. Gobbi, A. Pascual, F. Golmar, R. Llopi, P. Vavassori, F. Casanova, L.E. Hueso, C 60/NiFe combination as a promising platform for molecular spintronics, *Org. Electron. Physics, Mater. Appl.* 13 (2012) 366–372. doi:10.1016/j.orgel.2011.12.002.
- [66] M. Gobbi, F. Golmar, R. Llopi, F. Casanova, L.E. Hueso, Room-temperature spin transport in C60-based spin valves., *Adv. Mater.* 23 (2011) 1609–1613. doi:10.1002/adma.201004672.
- [67] D. Çakır, D.M. Otálvaro, G. Brocks, Magnetoresistance in multilayer fullerene spin valves: A first-principles study, *Phys. Rev. B.* 90 (2014) 245404. doi:10.1103/PhysRevB.90.245404.
- [68] S. Sakai, I. Sugai, S. Mitani, K. Takanashi, Y. Matsumoto, H. Naramoto, P. V. Avramov, S. Okayasu, Y. Maeda, Giant tunnel magnetoresistance in codeposited fullerene-cobalt films in the low bias-voltage regime, *Appl. Phys. Lett.* 91 (2007) 242104. doi:10.1063/1.2822397.
- [69] T.L.A. Tran, T.Q. Le, J.G.M. Sanderink, W.G. van der Wiel, M.P. de Jong, The Multistep Tunneling Analogue of Conductivity Mismatch in Organic Spin Valves, *Adv. Funct. Mater.* 22 (2012) 1180–1189. doi:10.1002/adfm.201102584.
- [70] X. Zhang, S. Mizukami, T. Kubota, Q. Ma, M. Oogane, H. Naganuma, Y. Ando, T. Miyazaki, Observation of a large spin-dependent transport length in

- organic spin valves at room temperature., *Nat. Commun.* 4 (2013) 1392.
doi:10.1038/ncomms2423.
- [71] M. Gobbi, A. Pascual, F. Golmar, R. Llopis, P. Vavassori, F. Casanova, L.E. Hueso, C₆₀/NiFe combination as a promising platform for molecular spintronics, *Org. Electron.* 13 (2012) 366–372.
doi:10.1016/j.orgel.2011.12.002.
- [72] F. Li, T. Li, F. Chen, F. Zhang, Spin injection and transport in organic spin-valves based on fullerene C₆₀, *Org. Electron. Physics, Mater. Appl.* 15 (2014) 1657–1663. doi:10.1016/j.orgel.2014.03.016.
- [73] F. Li, Effect of substrate temperature on the spin transport properties in C₆₀-based spin valves., *ACS Appl. Mater. Interfaces.* 5 (2013) 8099–104.
doi:10.1021/am402178w.
- [74] R. Lin, F. Wang, M. Wohlgemant, C. He, X. Zhai, Y. Suzuki, Organic spin-valves based on fullerene C₆₀, *Synth. Met.* 161 (2011) 553–557.
doi:10.1016/j.synthmet.2010.11.012.
- [75] X.Q. Shi, A.B. Pang, K.L. Man, R.Q. Zhang, C. Minot, M.S. Altman, M.A. Van Hove, C₆₀ on the Pt(111) surface: Structural tuning of electronic properties, *Phys. Rev. B.* 84 (2011) 235406.
doi:10.1103/PhysRevB.84.235406.
- [76] X.-Q. Shi, M.A. Van Hove, R.-Q. Zhang, Survey of structural and electronic properties of C₆₀ on close-packed metal surfaces, *J. Mater. Sci.* 47 (2012) 7341–7355. doi:10.1007/s10853-012-6361-y.
- [77] X.-Q. Shi, M.A. Van Hove, R.-Q. Zhang, Adsorbate-induced reconstruction by C₆₀ on close-packed metal surfaces: Mechanism for different types of reconstruction, *Phys. Rev. B.* 85 (2012) 75421.
doi:10.1103/PhysRevB.85.075421.
- [78] G. Xu, X.-Q. Shi, R.Q. Zhang, W.W. Pai, H.T. Jeng, M.A. Van Hove, Detailed low-energy electron diffraction analysis of the (4×4) surface

- structure of C₆₀ on Cu(111): Seven-atom-vacancy reconstruction, *Phys. Rev. B.* 86 (2012) 75419. doi:10.1103/PhysRevB.86.075419.
- [79] L. Tang, X. Zhang, Q. Guo, Y.-N. Wu, L.-L. Wang, H.-P. Cheng, Two bonding configurations for individually adsorbed C₆₀ molecules on Au(111), *Phys. Rev. B.* 82 (2010) 125414. doi:10.1103/PhysRevB.82.125414.
- [80] Z.-H. Yang, R. Pang, X.-Q. Shi, Engineering Magnetic Hybridization at Organic–Ferromagnetic Interfaces by C₆₀-Adsorption-Induced Fe(001) Surface Reconstruction, *J. Phys. Chem. C.* 119 (2015) 10532–10537. doi:10.1021/acs.jpcc.5b03954.
- [81] T.L.A. Tran, P.K.J. Wong, M.P. de Jong, W.G. van der Wiel, Y.Q. Zhan, M. Fahlman, Hybridization-induced oscillatory magnetic polarization of C₆₀ orbitals at the C₆₀/Fe(001) interface, *Appl. Phys. Lett.* 98 (2011) 222505. doi:10.1063/1.3595269.
- [82] T.L.A. Tran, D. Çakır, P.K.J. Wong, A.B. Preobrajenski, G. Brocks, W.G. van der Wiel, M.P. de Jong, Magnetic Properties of bcc-Fe(001)/C₆₀ Interfaces for Organic Spintronics, *ACS Appl. Mater. Interfaces.* 5 (2013) 837–841. doi:10.1021/am3024367.
- [83] S. Liang, R. Geng, B. Yang, W. Zhao, R. Chandra Subedi, X. Li, X. Han, T.D. Nguyen, Curvature-enhanced Spin-orbit Coupling and Spinterface Effect in Fullerene-based Spin Valves., *Sci. Rep.* 6 (2016) 19461. doi:10.1038/srep19461.
- [84] J. Krempaský, V.N. Strocov, L. Patthey, P.R. Willmott, R. Herger, M. Falub, P. Blaha, M. Hoesch, V. Petrov, M.C. Richter, O. Heckmann, K. Hricovini, Effects of three-dimensional band structure in angle- and spin-resolved photoemission from half-metallic La_{2/3}Sr_{1/3}MnO₃, *Phys. Rev. B.* 77 (2008) 165120. doi:10.1103/PhysRevB.77.165120.
- [85] B. Nadgorny, The case against half-metallicity in La_{0.7}Sr_{0.3}MnO₃, *J.*

- Phys. Condens. Matter. 19 (2007) 315209. doi:10.1088/0953-8984/19/31/315209.
- [86] T.D. Nguyen, F. Wang, X.-G. Li, E. Ehrenfreund, Z.V. Vardeny, Spin diffusion in fullerene-based devices: Morphology effect, Phys. Rev. B. 87 (2013) 75205. doi:10.1103/PhysRevB.87.075205.
- [87] H. Xie, D. Niu, L. Lyu, H. Zhang, Y. Zhang, P. Liu, P. Wang, D. Wu, Y. Gao, Evolution of the electronic structure of C₆₀/La_{0.67}Sr_{0.33}MnO₃ interface, Appl. Phys. Lett. 108 (2016) 11603. doi:10.1063/1.4939457.
- [88] L. Kyu Won, L. Cheol Eui, G. A., S. E., K. Yu., Triggering a Metal-insulator Transition in La_{0.8}Sr_{0.2}MnO₃ Nanoparticle-decorated Carbon Nanotubes, J. Korean Phys. Soc. 59 (2011) 3309. doi:10.3938/jkps.59.3309.
- [89] S.C. Ray, H.M. Tsai, H.C. Chen, S.L. Wu, D.C. Ling, I.N. Lin, W.F. Pong, Electronic structure, electron field emission and magnetic behaviors of carbon nanotubes fabricated on La_{0.66}Sr_{0.33}MnO₃ (LSMO) for spintronics application, J Nanosci Nanotechnol. 11 (2011) 10710–10714.
http://www.ncbi.nlm.nih.gov/entrez/query.fcgi?cmd=Retrieve&db=PubMed&dopt=Citation&list_uids=22408979.
- [90] K. Miyazaki, K. Kawakita, T. Abe, T. Fukutsuka, K. Kojima, Z. Ogumi, Single-step synthesis of nano-sized perovskite-type oxide/carbon nanotube composites and their electrocatalytic oxygen-reduction activities, J. Mater. Chem. 21 (2011) 1913. doi:10.1039/c0jm02600j.
- [91] L.E. Hueso, G. Burnell, J.L. Prieto, L. Granja, C. Bell, D.J. Kang, M. Chhowalla, S.N. Cha, J.E. Jang, G.A.J. Amaratunga, N.D. Mathur, Electrical transport between epitaxial manganites and carbon nanotubes, Appl. Phys. Lett. 88 (2006) 6–8. doi:10.1063/1.2170431.
- [92] L.E. Hueso, J.M. Pruneda, V. Ferrari, G. Burnell, J.P. Valdés-Herrera, B.D. Simons, P.B. Littlewood, E. Artacho, A. Fert, N.D. Mathur, Transformation of spin information into large electrical signals using carbon nanotubes.,

- Nature. 445 (2007) 410–413. doi:10.1038/nature05507.
- [93] G. Kresse, J. Furthmüller, Efficiency of ab-initio total energy calculations for metals and semiconductors using a plane-wave basis set, *Comput. Mater. Sci.* 6 (1996) 15–50. doi:10.1016/0927-0256(96)00008-0.
 - [94] G. Kresse, J. Furthmüller, Efficient iterative schemes for *ab initio* total-energy calculations using a plane-wave basis set, *Phys. Rev. B.* 54 (1996) 11169–11186. doi:10.1103/PhysRevB.54.11169.
 - [95] G. Kresse, J. Hafner, *Ab initio* molecular-dynamics simulation of the liquid-metal–amorphous-semiconductor transition in germanium, *Phys. Rev. B.* 49 (1994) 14251–14269. doi:10.1103/PhysRevB.49.14251.
 - [96] G. Kresse, J. Hafner, *Ab initio* molecular dynamics for liquid metals, *Phys. Rev. B.* 47 (1993) 558–561. doi:10.1103/PhysRevB.47.558.
 - [97] G. Kresse, J. Hafner, Norm-conserving and ultrasoft pseudopotentials for first-row and transition elements, *J. Phys. Condens. Matter.* 6 (1994) 8245–8257. doi:10.1088/0953-8984/6/40/015.
 - [98] J.P. Perdew, J.A. Chevary, S.H. Vosko, K.A. Jackson, M.R. Pederson, D.J. Singh, C. Fiolhais, Atoms, molecules, solids, and surfaces: Applications of the generalized gradient approximation for exchange and correlation, *Phys. Rev. B.* 46 (1992) 6671–6687. doi:10.1103/PhysRevB.46.6671.
 - [99] J.P. Perdew, J.A. Chevary, S.H. Vosko, K.A. Jackson, M.R. Pederson, D.J. Singh, C. Fiolhais, Erratum: Atoms, molecules, solids, and surfaces: Applications of the generalized gradient approximation for exchange and correlation, *Phys. Rev. B.* 48 (1993) 4978–4978. doi:10.1103/PhysRevB.48.4978.2.
 - [100] G. Kresse, D. Joubert, From ultrasoft pseudopotentials to the projector augmented-wave method, *Phys. Rev. B.* 59 (1999) 1758–1775. doi:10.1103/PhysRevB.59.1758.
 - [101] H.J. Monkhorst, J.D. Pack, Special points for Brillouin-zone integrations,

- Phys. Rev. B. 13 (1976) 5188–5192. doi:10.1103/PhysRevB.13.5188.
- [102] W. Krätschmer, L.D. Lamb, K. Fostiropoulos, D.R. Huffman, Solid C60: a new form of carbon, *Nature*. 347 (1990) 354–358. doi:10.1038/347354a0.
- [103] V.I. Anisimov, J. Zaanen, O.K. Andersen, Band theory and Mott insulators: Hubbard U instead of Stoner I , *Phys. Rev. B*. 44 (1991) 943–954. doi:10.1103/PhysRevB.44.943.
- [104] P.E. Blöchl, Projector augmented-wave method, *Phys. Rev. B*. 50 (1994) 17953–17979. doi:10.1103/PhysRevB.50.17953.
- [105] C. Ma, Z. Yang, S. Picozzi, Ab initio electronic and magnetic structure in $\text{La}_{0.66}\text{Sr}_{0.33}\text{MnO}_3$: strain and correlation effects., *J. Phys. Condens. Matter*. 18 (2006) 7717–28. doi:10.1088/0953-8984/18/32/019.
- [106] S. Picozzi, C. Ma, Z. Yang, R. Bertacco, M. Cantoni, A. Cattoni, D. Petti, S. Brivio, F. Ciccacci, Oxygen vacancies and induced changes in the electronic and magnetic structures of $\text{La}_{0.66}\text{Sr}_{0.33}\text{MnO}_3$: A combined ab initio and photoemission study, *Phys. Rev. B*. 75 (2007) 94418. doi:10.1103/PhysRevB.75.094418.
- [107] B. Zheng, N. Binggeli, Influence of the interface atomic structure on the magnetic and electronic properties of $\text{La}_{2/3}\text{Sr}_{1/3}\text{MnO}_3/\text{SrTiO}_3$ (001) heterojunctions, *Phys. Rev. B*. 82 (2010) 245311. doi:10.1103/PhysRevB.82.245311.
- [108] M.C. Martin, G. Shirane, Y. Endoh, K. Hirota, Y. Moritomo, Y. Tokura, Magnetism and structural distortion in the $\text{La}_{0.7}\text{Sr}_{0.3}\text{MnO}_3$ metallic ferromagnet, *Phys. Rev. B*. 53 (1996) 14285–14290. doi:10.1103/PhysRevB.53.14285.
- [109] F. Tsui, M.C. Smoak, T.K. Nath, C.B. Eom, Strain-dependent magnetic phase diagram of epitaxial $\text{La}_{0.67}\text{Sr}_{0.33}\text{MnO}_3$ thin films, *Appl. Phys. Lett.* 76 (2000) 2421. doi:10.1063/1.126363.
- [110] W. Tang, E. Sanville, G. Henkelman, A grid-based Bader analysis algorithm

- without lattice bias., *J. Phys. Condens. Matter.* 21 (2009) 84204.
doi:10.1088/0953-8984/21/8/084204.
- [111] E. Sanville, S.D. Kenny, R. Smith, G. Henkelman, Improved grid-based algorithm for Bader charge allocation, *J. Comput. Chem.* 28 (2007) 899–908.
doi:10.1002/jcc.20575.
- [112] G. Henkelman, A. Arnaldsson, H. Jónsson, A fast and robust algorithm for Bader decomposition of charge density, *Comput. Mater. Sci.* (2006).
<http://www.sciencedirect.com/science/article/pii/S0927025605001849>
(accessed July 21, 2016).
- [113] H. Nejat Pishkenari, A. Nemati, A. Meghdari, S. Sohrabpour, A close look at the motion of C60 on gold, *Curr. Appl. Phys.* 15 (2015) 1402–1411.
doi:10.1016/j.cap.2015.08.003.
- [114] A.A. Kuzubov, E.A. Kovaleva, P. V. Avramov, A.S. Kholobina, N.S. Mikhaleva, A. V. Kuklin, Buckminsterfullerene's movability on the Fe(001) surface, *J. Magn. Magn. Mater.* 410 (2016) 41–46.
doi:10.1016/j.jmmm.2016.03.023.
- [115] A.A. Kuzubov, E.A. Kovaleva, F.N. Tomilin, N.S. Mikhaleva, A. V. Kuklin, On the possibility of contact-induced spin polarization in interfaces of armchair nanotubes with transition metal substrates, *J. Magn. Magn. Mater.* 396 (2015) 102–105.
- [116] E.A. Kovaleva, A.A. Kuzubov, P.V. Avramov, A.V. Kuklin, N.S. Mikhaleva, P.O. Krasnov, Characterization of LSMO/C60 spinterface by first-principle calculations, *Org. Electron.* 37 (2016) 55–60.
doi:10.1016/j.orgel.2016.06.021.